CAMBRIDGE
UNIVERSITY PRESS

Article

Mineralogical classification and crystal water characterisation of beryl from the W–Sn–Be occurrence of Xuebaoding, Sichuan province, western China

Ping Wang[1],[§], Thomas P. Gray[2], Zhe Li[3], Evan J.D. Anderson[2], Julien Allaz[4], Joseph R. Smyth[5], Alan E. Koenig[6],[†],
Lijian Qi[7], Yan Zhou[7] and Markus B. Raschke[2]* (ORCID)

[1]College of Physics, Sichuan University, Chengdu, Sichuan, 610064, China; [2]Department of Physics, Department of Chemistry, and JILA, University of Colorado, Boulder, CO 80303, USA; [3]Institute of Fundamental and Frontier Sciences, University of Electronic Science and Technology of China, Chengdu, Sichuan, 610054, China; [4]ETH Zürich, Department of Earth Sciences, Institute of Geochemistry and Petrology, Clausiusstrasse 25, 8092 Zurich, Switzerland; [5]Department of Geological Sciences, University of Colorado, Boulder, CO 80303, USA; [6]United States Geological Survey, Geology, Geophysics, and Geochemistry Science Center, Lakewood, Colorado, USA; and [7]Laboratory of Gem and Technological Materials, Tongji University, Shanghai 200070, China

Abstract

Beryl from Xuebaoding, Sichuan Province, western China is known for its unusual tabular habit and W–Sn–Be paragenesis in a greisen-type deposit. The crystals are typically colourless transparent to pale blue, often with screw dislocations of hexagonal symmetry on the (0001) crystal faces. Combining electron microprobe analyses and laser ablation inductively coupled plasma mass spectrometry with single-crystal X-ray diffraction (XRD), correlated with Raman and micro-infrared (IR) spectroscopy and imaging, the crystal chemical characteristics are determined. The contents of Na^+ (0.24–0.38 atoms per formula unit (apfu)) and Li^+ up to 0.38 apfu are at the high end compared to beryl from other localities worldwide. Li^+ substitution for Be^{2+} on the tetrahedral (T2) site is predominantly charge balanced by Na^+ on the smaller channel (C2) site, with Na^+ ranging from 91.5% to 99.7% (apfu) of the sum of all other alkali elements. Cs^+ and minor Rb^+ and K^+ primarily charge balance the minor M^{2+} substitution for Al^{3+} at the A site; all iron at the A site is suggested to be trivalent. The *a* axis ranges from 9.2161(2) to 9.2171(4) Å, with unit-cell volume from 678.03(3) to 678.48(7) Å^3. The *c/a* ratio of 1.0002–1.0005 is characteristic for T2-type beryl with unit-cell parameters controlled primarily by Be^{2+} substitution. Transmission micro-IR vibrational spectroscopy and imaging identifies coordination of one or two water molecules to Na^+ (type IIs and type IId, respectively) as well as alkali free water (type I). Based on IR absorption cross section and XRD a C1 site water content of 0.4–0.5 apfu is derived, i.e. close to 50% site occupancy. Secondary crystal phases with a decrease in Fe and Mg, yet increase in Na, suggest early crystallisation of aquamarine, with goshenite being late. With similar crystal chemistry to beryl of columnar habit from other localities worldwide, the tabular habit of Xuebaoding beryl seems to be unrelated to chemical composition and alkali content.

Keywords: beryl, Xuebaoding, crystal chemistry, tabular habit, crystal water, infrared spectroscopy

Introduction

Background

Beryl as the most common beryllium mineral is of important geochemical significance in different geological contexts. Ideally $Be_3Al_2Si_6O_{18}$, beryl is a cyclosilicate mineral of hexagonal crystal structure. Six-membered rings of Si tetrahedra are linked by tetrahedrally coordinated Be^{2+} (T2 site) and octahedrally coordinated

Al^{3+} (A site) in planes parallel to (0001) (Aurisicchio *et al.*, 1988, 1994; Černý, 2002; Groat *et al.*, 2008). The rings form channels parallel to the crystallographic *c* axis, which in natural beryl typically contain variable amounts of primarily alkali cations and neutral molecules of water, CO_2 and CH_4 (Ginzburg, 1955; Wood and Nassau, 1968; Hawthorne and Černý, 1977; Aines and Rossman, 1984; Artioli *et al.*, 1993; Charoy *et al.*, 1996; Pankrath and Langer, 2002; Gatta *et al.*, 2006; Groat *et al.*, 2008; Fridrichová *et al.*, 2016). The accommodation of monovalent alkali cations on the two channel vacancy sites charge balances the substitution of divalent or trivalent cations (e.g. Mg^{2+}, $Fe^{2+/3+}$ or Mn^{2+}) for Al^{3+} at the A site, or the substitution of primarily Li^+ for Be^{2+} at the T2 site (Folinsbee, 1941; Wood and Nassau, 1968; Bakakin *et al.*, 1969; Hawthorne and Černý, 1977; Aurisicchio *et al.*, 1988). The smaller alkali Na^+ occupies the narrower channel site (C2/2b), while the larger K^+, Cs^+ or Rb^+ as well as H_2O and CO_2 prefer the wider channel site (C1/

[§]Present address: Institute of Regulatory Science for Medical Devices, Sichuan University, Chengdu, Sichuan, 610064, China

[†]Present address: Applied Spectra, Inc., West Sacramento, CA 95605, USA

*Author for correspondence: Markus B. Raschke, Email: markus.raschke@colorado.edu
Cite this article: Wang P., Gray T.P., Li Z., Anderson E.J.D., Allaz J., Smyth J.R., Koenig A.E., Qi L., Zhou Y. and Raschke M.B. (2021) Mineralogical classification and crystal water characterisation of beryl from the W–Sn–Be occurrence of Xuebaoding, Sichuan province, western China. *Mineralogical Magazine* 85, 172–188. https://doi.org/10.1180/mgm.2021.13

2a) (Aurisicchio *et al.*, 1994; Łodziński *et al.*, 2005; Fukuda and Shinoda, 2008). Pure beryl is colourless (var. goshenite), whereas different substitutions give rise to distinct colours of blue (var. aquamarine, Fe), green (var. emerald, Cr/V), yellow (var. heliodor, Fe) or pink (var. morganite, Mn) (Lum *et al.*, 2016; Tempesta *et al.*, 2020).

Following early ultraviolet (UV), visible, and IR spectroscopy (Wood and Nassau, 1967, 1968), the lattice position, molecular orientation, bonding state and dynamic behaviour of water in natural and synthetic beryl, and at variable temperatures, have been characterised spectroscopically (Kim *et al.*, 1995; Charoy *et al.*, 1996; Kolesov and Geiger, 2000; Łodziński *et al.*, 2005; Fukuda and Shinoda, 2008, 2011). Based on these studies, water on the C1/2a sites has been defined as type I or type II with a molecular dipole moment orientated perpendicular or parallel with respect to the *c* axis, respectively. In addition the preference for each type is controlled by the channel alkali content.

Xuebaoding beryl

One notable occurrence of beryl is the Xuebaoding greisen-type W–Sn–Be deposit in the Songpan–Ganzi (or Songpan–Garzê) orogenic belt in Sichuan Province, western China (Zhang *et al.*, 2014). Explored since the 1950s, the occurrence is known for scheelite, cassiterite and beryl of exceptional size and gem quality, with quartz, fluorite and minor apatite formed in a post-magmatic hydrothermal process (Lin *et al.*, 2000; Zhou *et al.*, 2002; Liu *et al.*, 2005). The abundant beryl is typically transparent and colourless to pale blue. In contrast to the common columnar prismatic habit of beryl parallel to the *c* axis, Xuebaoding beryl is primarily of tabular habit parallel to the basal pinacoid.

Even though a range of studies have addressed the gemmology (Qi *et al.*, 2001a, b, c, d) and mineralogy of beryl from Xuebaoding over more than two decades (Guo *et al.*, 2000a, b; Lin *et al.*, 2000; Ye *et al.*, 2001; Zhou *et al.*, 2002; Liu *et al.*, 2007, 2012), its crystal chemistry has not yet been well established with several analytical results either inconclusive or in part contradictory, leading to a confusing picture even about elementary questions of composition and structure. Further, contrasting hypotheses were proposed, with crystal growth controlled by defects and dislocations (Qi *et al.*, 2001b) or by high alkali content at the Be and channel sites (Liu *et al.*, 2012) being responsible for the tabular habit.

This work

The goal of this work is a systematic chemical, including trace element, and structural classification of beryl from Xuebaoding including comparison with beryl from other localities, notably of comparable tabular habit. Further, water in its different structural states and its vibrational response are quantified by correlating single-crystal X-ray diffraction with Raman and IR micro-spectroscopy and imaging.

Geographic and geological setting

The sample localities are generally referred to as Xuebaoding (Sichuan Province, China) situated northwest of the Longmen Shan range, at the eastern margin of the Tibetan plateau, at elevations of 3900–4200 m. The locality is named after the mountain Xuebaoding ('Snow Treasure Crown', Tibetan name: Shar Dung Ri, elevation 5,588 m), the highest peak of the Minshan range.

However, Xuebaoding mountain itself is 5.3 km to the NW of the locality, and not visible from the locality, separated by several high ridges and the mountain Sigenxiangfeng (5,360 m). Instead, the peak visible to the immediate NW (Fig. 1a, top left), is Little Xuebaoding (5,443 m) and situated above the valley to the western terminus of the locality area. The confusion between the two peaks, including confusion about first ascents of these mountains persisted well into the 1980s, and until today by the local population, as a reflection of the complex topography and extreme relative relief of up to 4000 m between the valley floors and adjacent peaks, with many of similar altitude.

Tectonically, the area is situated in the Songpan–Ganzi orogenic belt to the west of the Sichuan Province, near the contact with the Qinling orogenic belt (north) and the western Yangtze block (east and south-east) (Fig. 1b). The Songpan–Ganzi orogenic belt is the result of two stages of tectonic movements. Following the late Indochina tectonic epoch with long-term intracontinental convergence and associated series of magmatic and metamorphic events, the subsequent Himalayan movement starting at ~80 Ma resulted in a pronounced twist in the Songpan–Ganzi orogenic belt (Xu *et al.*, 1992; Kirby and Ouimet, 2011). Along the Minshan (or Min Mountains) the active fault system of the N–S trending Huya fault, a steeply west-dipping reverse fault, contributes to the ongoing uplift of the Minshan. The Huya fault separates Precambrian basement and overlying late Proterozoic to Permian rock units to its east, from the Triassic Songpan–Ganzi flysch sequences to its west (Kirby and Ouimet, 2011). The numerous intruded granites in the eastern margin of the Tibetan plateau have been dated at 220 to 188 Ma (Roger *et al.*, 2004, 2010; Xiao *et al.*, 2007).

Geology of the Xuebaoding deposit

The Xuebaoding mineralisation is associated with several Mesozoic leucogranite intrusions, of a few 100 m to 1 km in extent in outcrop (e.g. Pankou, Pukou and Wuzhutang), of similar spatial separation, and dated at 201–194 Ma (Fig. 1c) (Ye *et al.*, 2001; Zhou *et al.*, 2002; Cao *et al.*, 2004; Jiang *et al.*, 2007; Li *et al.*, 2007). Whether these different outcrops are of a single intrusion, or represent separate intrusions, and their relationship is yet unknown. However, their similarities in rock type and associated mineralisation suggests at least a close magmatic relationship.

The granites intruded into the upper Triassic Zhuwo series of deep-marine sedimentation origin, accompanied by slate, schist and marble lenticules, as well as layers of marble of shallow metamorphism of late Indosinian orogeny to early Yanshan age (Zhou *et al.*, 2002; Cao *et al.*, 2004; Ottens, 2005; Li *et al.*, 2007). The sequence of layers of sericite, quartz and carbonaceous schist, mudstone, marble and local skarn, are overturned, with shallow dip to the west, yet steeply dipping to the east of the granite contacts (Fig. 1c).

Mineral assemblage

The Xuebaoding locality is a globally significant occurrence of scheelite and cassiterite, in combination with beryl, all of unusually large size, gem colour, and crystal quality. It is a greisen-type deposit of quartz and muscovite. Albeit locally variable in relative distribution, the joint mineralisation of scheelite, cassiterite and beryl suggests that it is derived from a highly fractionated and evolved magma in the apical section of the granitic
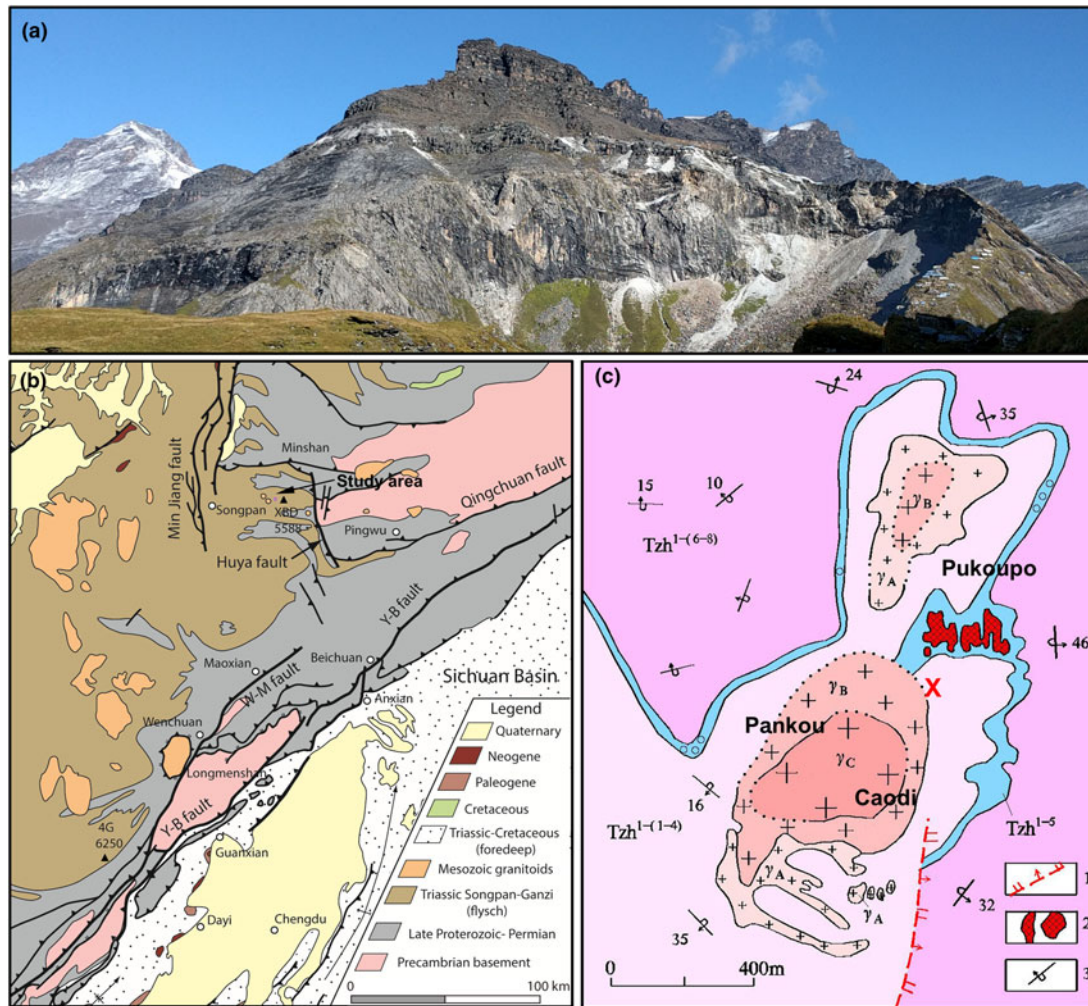
Fig. 1. (a) Xuebaoding locality, with Little Xuebaoding (5,443 m, left) in the background. Mineralised zones along a nearly horizontal marble band (white mine tailings) and in schist, along and below both sides of ridge to the right (mining camp at bottom right). (b) Generalised geological map of eastern margin of Tibetan plateau with Xuebaoding (XBD) mountain west of the Huya fault and to NE of the Longmen Shan range and uplift zone defined by Yingxiu–Beichuan (Y-B) and Wenchuan–Maoxian (W-M) faults; major peaks of Siguniangshan (4G) and Xuebaoding (XBD) indicated (modified with permission after Kirby and Ouimet, 2011). (c) Geological map of the main locality area (pink rectangle in (b)) associated with granite body outcrops Pankou and Caodi (defining the cirques in (a)) and Pukoupo. Legend: 1: normal fault, 2: highly mineralised quartz vein containing beryl, scheelite and cassiterite, 3: overturned dip and strike (modified after Zhou *et al.*, 2002). Rock units: $Tzh^{1-(1-4)}$ quartz schist, marble, biotite-quartz schist; Tzh^{1-5} ore-bearing strata, marble; $Tzh^{1-(6-8)}$ calcareous quartz schist, sericite quartz schist; γ_{A-C} granite margin through transition to core zone. The W–Sn–Be mineralisation is concentrated throughout schist and marble within <100 m from the granite intrusions. Approximate sample locations in vicinity and south of reference position (red cross: lat. 32.6121987°N, long. 103.9418417°E).

body (Cao *et al.*, 2002, 2004; Li *et al.*, 2007; Zhang *et al.*, 2014; Zhu *et al.*, 2020). Highly enriched in volatiles and metallic elements this gives rise to simple mineralisation of large, mostly common, W, Sn, Be, F and P minerals. The mineralisation of muscovite, with fluorite and apatite in addition to the W and Sn mineralisation is typical for an S-type granite derived system. The mineralisation is fracture-controlled and occurs in sheeted veins and stockwork, emanating from the greisenised granite into the country rock. However, associated post-magmatic alteration of the host rock by volatiles and solutions derived from the cooling granitic intrusion, as is otherwise typical for greisen, is not very pronounced (Aurisicchio *et al.*, 1994).

Forming interconnected networks of quartz (with muscovite and fluorite), well-defined mineralised veins with a N–S trend are found primarily in marble, with a more stockwork type in the surrounding schist. This reflects that the marble is more brittle forming fractures for fluids to circulate and deposit, with the schist more ductile. The different ore veins in granite, marble

and schist as host rock with different generations and conditions with spatial and temporal variations in mineralisation exhibit large variations in mineral assemblage – with locally spatial ring fractures, replacement mineral bodies, distal vein emplacement, hydrothermal breccia boiling and hydrothermal alterations.

Xuebaoding beryl

The global occurrence of beryl, especially in large crystals, is typically associated with granitic pegmatites. Tungsten and tin mineralisations often occur simultaneously and are associated, but typically without beryl. Mineralisation of W and Sn together with Be is generally uncommon, which makes the combination of W, Sn and Be mineralisation of the Xuebaoding occurrence, and not of a pegmatite-type but rather of a hydrothermal/greisen-type, make Xuebaoding unusual.

Despite decades of research since the discovery of the localities in the 1950s (Guo *et al.*, 2000a; Qi *et al.*, 2001b; Cao *et al.*, 2002;
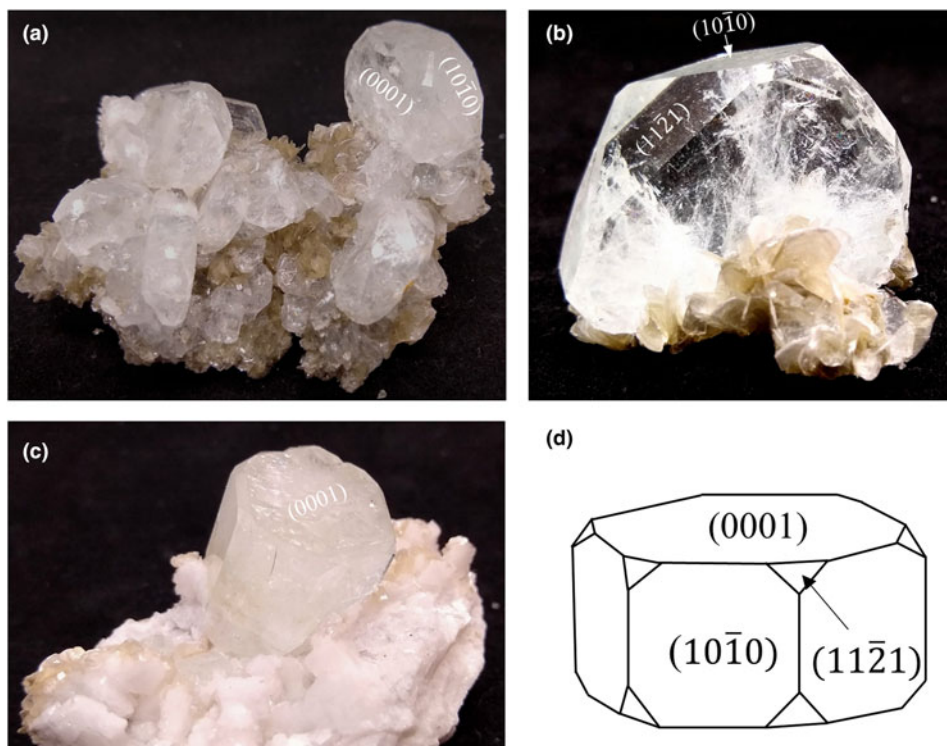
Fig. 2. Examples of representative Xuebaoding beryl habits: (a) cluster of tabular beryl on muscovite matrix (largest crystal 25 mm wide); (b) individual clear tabular crystal (40 mm wide); (c) rare columnar habit (on albite, 25 mm wide), light blue, with typical dislocation texture on (0001); (d) schematic of tabular habit.

Zhou et al., 2002; Liu et al., 2012; Zhang et al., 2012), only limited field studies have been undertaken and the ore-forming processes and source of the fluid are not yet clear. Further, despite several ages reported for granite and mineralisation, some are inconsistent, and it is unknown if they reflect the date of mineral formation.

Xuebaoding beryl is mostly colourless, transparent and rarely with a hint of blue. It typically exhibits a simple morphology, yet of characteristic tabular habit shortened in the c direction, with the most common basal pinacoid (0001), prisms $(10\bar{1}0)$ and $(11\bar{2}1)$ faces as shown in Fig. 2. The habit is rarely columnar, and if so has a low aspect ratio (Fig. 2c).

Numerous studies covering a wide range of techniques have addressed selected aspects of the crystal chemistry of beryl from Xuebaoding (Guo et al., 2000a; Qi et al., 2001b; Cao et al., 2002; Zhou et al., 2002; Liu et al., 2012; Zhang et al., 2012). Specifically, several studies using bulk chemical analysis, electron microprobe analysis (EPMA), and laser ablation inductively coupled plasma mass spectrometry (LA-ICP-MS) identified enrichment in Na^+ (Na_2O = 0.035–1.66 wt.%) and Li^+ (Li_2O = 0.63–3.04 wt.%) with variable amounts of Cs^+ (Cs_2O = 0.11–0.92 wt.%), and minor K^+ (K_2O = 0.01–1.13 wt.%), Mg^{2+} (MgO = 0.03–0.13 wt.%), Ca^{2+} (CaO = 0.01–0.88 wt.%) and Fe^{3+} (FeO_T = 0.06–0.54 wt.%) (Liu et al., 2001b, 2005, 2012; Qi et al., 2001b; Zhou et al., 2002; literature data summarised in Supplementary Table S1). While some analyses are inconsistent, they confirm the trend that defines Xuebaoding beryl as a lithium–sodium or 'tetrahedron' beryl (Aurisicchio et al., 1988, 1994)

A comprehensive EMPA of beryl, whole rock analysis of granite, and fluid inclusion study suggested a post-magmatic pneumatolytic–hydrothermal solution as the source of the beryl mineralisation (Zhou et al., 2002). An X-ray fluorescence and LA-ICP-MS trace-element analysis, in combination with XRD, and surface textural features, identified Li^+ substitution at the tetrahedral Be^{2+} site together with divalent cation substitution for Al^{3+} with associated charge balancing by other alkali on the vacancy site (Liu et al., 2012). The high alkali content (0.255–0.327 apfu, not including Li^+) was hypothesised to be responsible for the tabular crystal growth (Liu et al., 2012). In contrast, a detailed analysis of surface defects on different crystal phases in combination with a growth rate model as a function of supersaturation (Qi et al., 2001b) suggested interstitial deformation and dislocation sliding responsible for the different growth rate of basal vs. prismatic crystal faces giving rise to the tabular morphology (Zhang et al., 2012).

Several fluid-inclusion studies have been performed for quartz, beryl and scheelite identifying homogenisation temperatures covering a wide range of 214–288°C (Cao et al., 2002), 158–310°C (Zhou et al., 2002), 250–292°C (Chen et al., 2002), 265–315°C (Lin et al., 2000), 188–373°C (Zhang et al., 2012) and 266–389°C (Liu et al., 2005), suggesting a shallow hydrothermal quartz vein type system. These works imply a volatile-rich pneumatolytic–hydrothermal solution derived from post-magmatic fluid as a source of the mineralisation (Cao et al., 2002; Zhou et al., 2002). Related work suggests a temperature range of 250–292°C, at high pressures (~86 MPa) with high CO_2 density (0.662 g/cm^3), and low salinity (6.191 wt.% NaCl) during the formation of beryl (Chen et al., 2002). This is consistent with more recent work (Zhang et al., 2012) suggesting a temperature of beryl formation of ~300°C.

Material and analytical methods

For this study selected single crystals and rock-forming beryl were chosen from different veins and collected in situ. The rock-forming sample hosted in quartz schist Tzh$^{1-(1-4)}$ has been extracted from an active mine on the east side of Pankou (thin section 1702B2, for details see Supplementary Fig. S1). Further, from clefts in veins hosted in marble Tzh$^{1-5}$ small single crystals of 0.5–1.5 cm
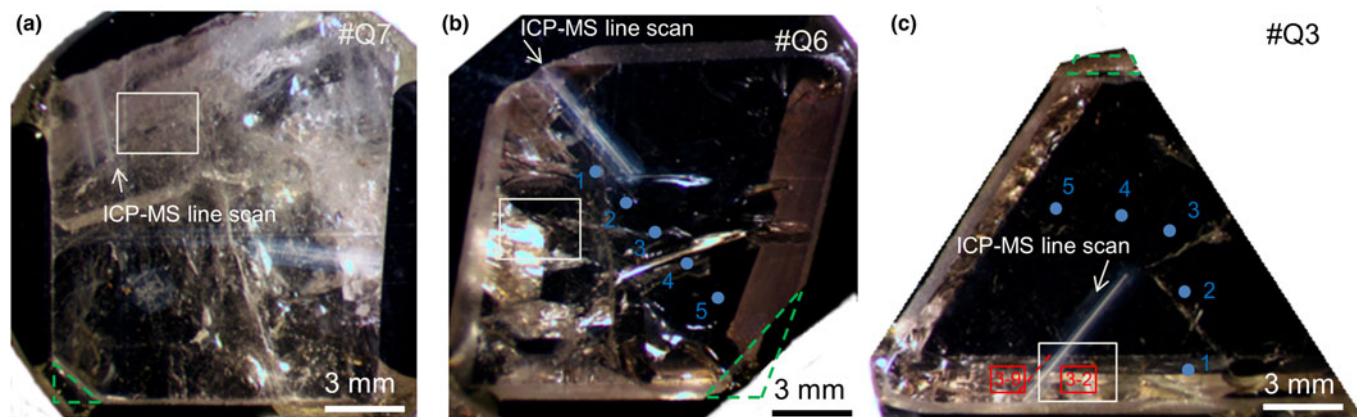
Fig. 3. Beryl samples as cut and studied from larger single crystal specimens: (a) #Q7, (0001) faces; (b) #Q6, (11$\bar{2}$1) faces; and (c) #Q3, (10$\bar{1}$0) faces. Indicated are positions of LA-ICP-MS transects (white arrows, Fig. 7), BSE imaging (white rectangles, Fig. 7), micro-IR transects and mapping (red dashed line and rectangles, Figs. 10–12), XRD (chips cut at dashed green triangles) and EMPA (blue dots).

in size were obtained and cut into thin sections, with two samples cut parallel and four perpendicular with respect to the *c* axis (1901B1 and 1901B2, for details see Fig. S1). Lastly several single crystals were collected from open space in veins in the northern area of Pankou (#Q1–Q7, see Fig. S1). The different crystal faces were first studied by atomic force microscopy (AFM, AIST Inc., noncontact mode, probe tips from μMasch Inc., spatial resolution ~10 nm and sample scanner resolution 2 nm), prior the preparation of slabs of 2–3 mm thickness for EMPA cut along different crystallographic directions perpendicular to (0001), (10$\bar{1}$0) and (11$\bar{2}$1) (#Q7, #Q3 and #Q6), as shown in Fig. 3. Subsequently for IR transmission spectroscopy and imaging, the samples were thinned to ~0.1 mm double sided polished slabs.

Micro-scale compositional mapping and quantitative microanalyses were undertaken with a JEOL JXA-8230 electron microprobe at the University of Colorado, USA (Department of Geological Sciences). It is a five-spectrometer instrument equipped with argon X-ray detectors (P-10 mixture) on spectrometer 1 and 2, and xenon X-ray detectors on spectrometers 3 to 5. Analytical conditions were 15 kV and 20 nA with a 5 μm beam diameter (samples XBD 19-01-B1 and 17-02-B2). Background positions were chosen to avoid interferences. In order to improve precision, a few additional analyses were performed at 50 nA and 10 μm beam diameter (samples #Q7, #Q6 and #Q3). The mean atomic number background correlation was used for all analyses (Donovan *et al.*, 2016). Counting time was optimised to improve the detection limit. The ZAF matrix correction from Armstrong (1988) using the FFAST mass absorption coefficient table (Chantler *et al.*, 2005) was applied throughout. Typical detection limits are ~0.01 wt.% for main and minor elements.

Minor and trace elements were measured by LA-ICP-MS at the USGS Denver Federal Center, USA. Three beryl crystals with representative primary and secondary crystal phases based on the EMPA were selected. A Photon Machines Analyte G2 LA system (193 nm and 4 ns excimer) was coupled to a PerkinElmer DRC-e ICP-MS. Spot-lined analyses were carried out for known locations, crossing the primary and secondary phase zones. A wavelength of 193 nm was used. Ablation was carried out using an 80-μm square spot size at 12 J/cm^2. Single spot analyses were ablated using 15 pulses/sec (15 Hz). Signals were calibrated using USGS synthetic basalt glass GSE-1g. Silicon

(29Si) was used as the internal standard element (using an average Si wt.% content from EMPA data) for concentration calculations (Pauly, 2019).

For X-ray diffraction and structure refinement, fragments were cut from crystals #Q3, #Q6 and #Q7. Single-crystal X-ray diffraction data were acquired on a Brucker P4 four-circle diffractometer (University of Colorado, USA) equipped with a point detector, an APEX II CCD detector, and a rotating Mo-anode generator operating at 50 kV and 250 mA. Unit-cell parameters were refined using the point-detector. The program *SHELXL-97* (Sheldrick, 2008) was used to analyse the site occupancies.

Micro-Raman spectroscopy on polished sections and oriented crystals was performed on a setup (XploRA Nano, Horiba Jobin Yvon) based on a confocal Raman microscope, using 532 nm excitation, a 50× objective (NA = 0.5 and focus size ≈1 μm diameter), with power on sample of ~3 mW. Spectra are acquired using a grating of 1800 grooves/mm providing for a spectral resolution of 0.5 cm^{-1}, with a thermoelectrically cooled CCD camera. The phonon response of silicon at 520.7 cm^{-1} was used to calibrate the spectrometer.

Unpolarised micro-IR spectroscopy and imaging was performed in transmission, reflection and attenuated-total reflection mode (FTIR microscope LUMOS, Bruker Inc.). Background spectra were recorded before the sample measurements in air and subtracted to obtain absorbance spectra of the samples. Measurements were performed in transmission on the double-sided polished crystal slabs of 120 μm thickness or less, with 50 μm spatial resolution, and 2 cm^{-1} spectral resolution from 800 cm^{-1} to 6000 cm^{-1}. Point spectra, line scans and images were acquired after EMPA and LA-ICP-MS and in areas of close proximity to correlate the CO_2 and H_2O IR spectra with the elemental crystal composition. For infrared peak frequencies and mode assignment see Table S2.

Results

Surface texture

Optical microscopy and AFM were used to study the beryl surface texture, notably of the (0001), (10$\bar{1}$0) and (11$\bar{2}$1) crystal faces. As established previously (Qi *et al.*, 2001b), the (0001) face shows hexagonal protrusions representing screw dislocations (Fig. 4a, e).
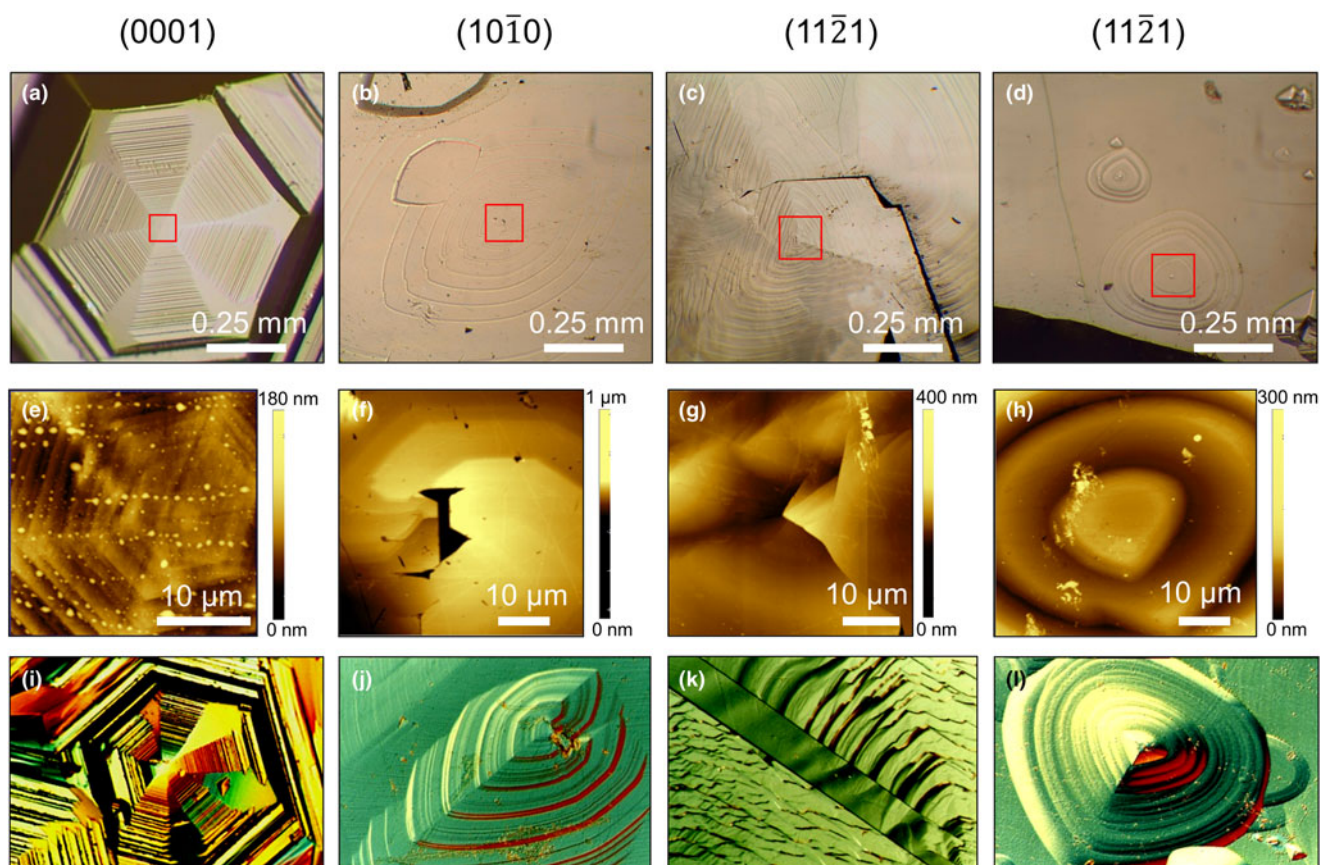
Fig. 4. Surface texture of different crystal faces of Xuebaoding beryl. (a–d) Unpolarised optical microscope images of #Q7, #Q3, #Q6 and #Q5, respectively. (e-f) AFM images of areas indicated in (a–d) (red square). (i–l) Differential interference microscope images of similar defects on corresponding faces [modified after Qi et al., 2001a]. (a, e, i) are (0001) faces, (b, f, j) are (10$\bar{1}$0) faces, and (c, d, g, h, k, l) are (11$\bar{2}$1) faces.

Most of the hexagonal screw dislocations in (0001) display finely spaced growth steps. The (10$\bar{1}$0) faces are dominated by left-handed or right-handed screw dislocations of nearly rhombohedral shape with long axis approximately parallel with respect to (0001) (Fig. 4b, f). The screw dislocations grow from the nucleation site in spirals outwards (Qi et al., 2001b). The lower density of the screw steps and kinks on (10$\bar{1}$0) compared to (0001) indicates a more rapid crystal growth in the (10$\bar{1}$0) lattice plane compared to (0001) leading to the tabular crystal habit (Qi et al., 2001b). In some (11$\bar{2}$1) lattice planes of beryl (Fig. 4c, g), the stacking fault defects grow layer-by-layer, until they cover the entire crystal face. Eventually, a step source that no longer disappears is formed at the protrusion of the stacking fault. The stacking fault also acts as the nucleus of the contract twin (Fig. 4k) (Qi et al., 2001b). Occasionally, dispersed heart-shaped step bunching is observed. The dislocation step spirals outwards from the protrusion and forms a closed spiral (Fig. 4d, h). A detailed future study of defects, dislocations and other structural bulk and surface features may possibly relate these features to crystal morphology and growth environment (Sunagawa, 1984; Scandale et al., 1990; Scandale and Lucchesi, 2000; Tempesta et al., 2011).

Chemical composition

Figure 5 shows optical and EMPA of the narrow vein (thin section 1702B2) containing scheelite at the schist contact and beryl in muscovite (Fig. 5a plain light, Fig. 5b UV with scheelite grain fluorescence). The beryl exhibits complex zoning as seen in the example of Fig. 5c (corresponding back-scattered electron (BSE) image Fig. 5d). Quantitative compositional element mapping of Al, Na, Fe and Cs (Fig. 5e–h, in oxide wt.%) indicates the negative correlation of Al and Fe, representing the substitution of Al^{3+} for $M^{2+/3+}$ cations, and the corresponding positive correlation of Al^{3+} with Na^+ and Cs^+ for charge balance.

Results of EMPA of seven representative zones averaged over three points of 1702B2 (for details see Fig. 5 and 6: low Na^+, circles; high Na^+, squares; intermediate Na^+, triangle), as well as analyses of samples 1901B and #Q7 (see analysis points in Figs S2, S3) are summarised in Table 1 and cover the range of compositional variations observed. SiO_2 values range from 64.22 to 65.04 wt.% (ideal 67.07 wt.%) and Al_2O_3 values range from 17.81 to 18.55 wt.% (ideal 18.97 wt.%). Of the minor elements, Na_2O dominates, ranging from 1.23 wt.% up to 2.01 wt.% and Cs_2O up to 0.49 wt.%. Iron as FeO_T (total Fe reported as FeO) ranges up to 0.50 wt.%, and MgO up to 0.19 wt.%. Traces of K^+, Ca^{2+}, Ti^{4+} and Mn^{2+} are close to the detection limit of ~0.01 wt.%.

The EMPA calculations (Table 1) are based on 18 O apfu and 3 [Be + Li]. LA-ICP-MS revealed a close correlation between Li^+ and Na^+, allowing for the use of Na^+ as a proxy for Li^+ to a good approximation. Be^{2+} is thus assumed to be 3 – Li^+. For comparison, calculations on the basis of either 18 O and 3 Be, or 6 Si are shown in Table S3 and S4, respectively (Groat et al., 2008; Fridrichová et al., 2016; Lum et al., 2016).
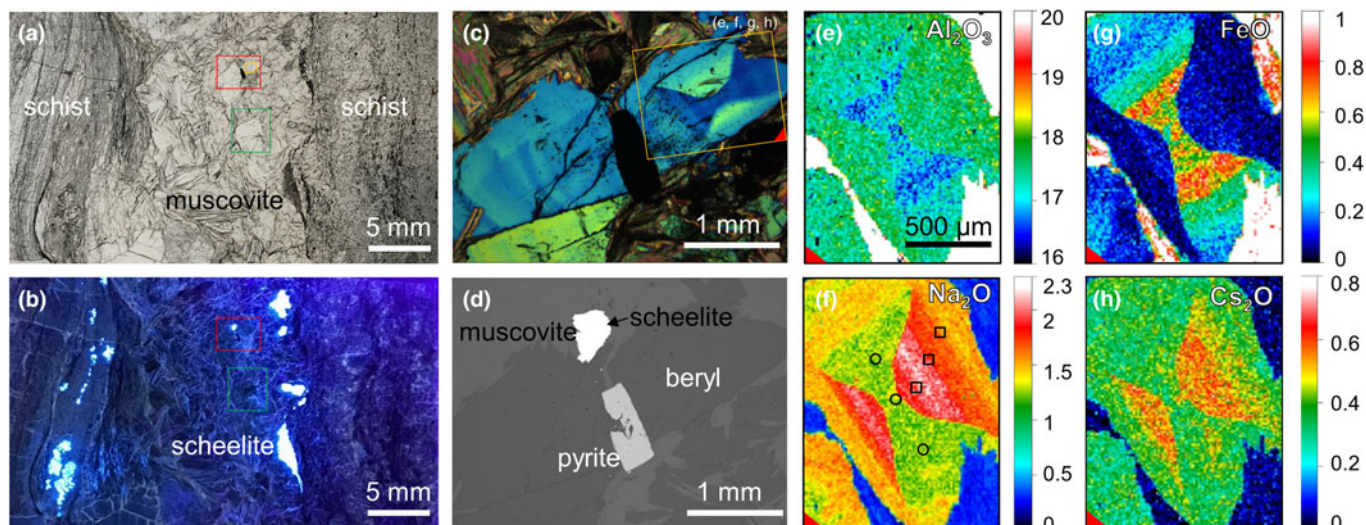
Fig. 5. Narrow vein of muscovite in schist with scheelite and beryl (thin section 1702B2): (a) plane light; (b) UV light; (c) beryl under crossed polarised light (red area from a); (d) corresponding BSE image. Quantitative EMPA mapping (scale bar oxide wt.%) of Al_2O_3 (e), Na_2O (f), FeO (g) and Cs_2O (h) of yellow region indicated in (c) with zoning and coupled substitution. Data for EMP point analyses (open circles and squares in (f)) in Table 1. For BSE and EMPA data of second area (green rectangles in (a) and (b)) see Fig. 6.

With Si^{4+} ranging from 5.978 to 5.994 apfu this indicates almost full 6 Si T1 site occupation without Si–Al substitution. Na^+ ranges from 0.20 to 0.36 apfu, which is much higher than Mg^{2+} (up to 0.027), K^+ (0.001–0.004), Cs^+ (0.004–0.019), Ca^{2+} (<0.002), Ti^{4+} (<0.002), Fe^{3+} (up to 0.034) and Mn^{2+} (<0.002). Na^+ typically occupies the channel site to balance the charge difference by coupled substitution.

Data from LA-ICP-MS was used to determine Li^+ and other minor and trace elements. Representative results of LA-ICP-MS line scans in samples #Q7, #Q6 and #Q3 are shown in Figure 7, highlighting regions of primary concentric zoning dissected by secondary veinlets (#Q7, Fig. 7a), typical primary concentric zoning (#Q6, Fig. 7b), or irregular but zoned regions near a crystal surface (#Q3, Fig. 7c), with corresponding LA-ICP-MS transects (Fig. 7d–f) as indicated. A characteristic and correlated increase in Na^+ and Li^+ is observed in the secondary phases, with corresponding depletion in K^+, Rb^+, Cs^+, Mg^{2+}, Mn^{2+} and Fe^{3+}. This effect is reflected in the BSE contrast in primary as well as secondary growth darker areas corresponding to greater light element content of Li^+ and Na^+, with depletion in the heavy elements.

Representative quantitative LA-ICP-MS results are listed in Table 2, with calculated apfu values based on assuming 6 Si. Consistent with EMPA results, Na^+ ranges from 0.25 to 0.37 apfu, compared to minor Cs^+ (0.0035–0.016), Mg^{2+} (0.000–0.017), Fe^{3+} (0.000–0.015) and only traces of other elements. In the primary zones, Na^+ (0.246–0.268) is considerably less than in the secondary zones (0.354–0.371), yet correlated closely with the amount of Li^+ in primary (0.254–0.272) and secondary beryl (0.347–0.368).

In summary, these results show the presence of only a weak Al^{3+} A-site for 2+ cations substitution vector, but a dominating Li^+ T2-site for Be^{2+} substitution vector (see discussion below).

Crystallography and structure refinement

The refined crystal structure parameters as well as data collection parameters, are summarised in Table 3. The unit-cell parameters were refined from centring angles of 60 strong reflections with two between 10 and 28° using a point detector system on a Bruker P4 diffractometer. The *a*-axis values of the lattice range from 9.2161(2) to 9.2171(4) Å, while *c*-axis values range from 9.2178(2) to 9.2219(4) Å, and the unit-cell volume ranges from 678.03(3) to 678.48(7) Å³. The *c/a* ratio ranges from 1.0002 to 1.0005 and is consistent with T2 type beryl, with the unit-cell controlled primarily by Be^{2+} substitution (Aurisicchio *et al.*, 1988, 1994). Intensity data were measured using a Bruker APEX II CCD detector out to a two-theta angle of ~80° (Table 3). Atom position, displacement parameters and cation occupancies were refined using *SHELXL* (Sheldrick, 2008) based on ionised atom scattering factors for cations (Cromer and Mann, 1968) and O^{-2} (Azavant and Lichanot, 1993). Atom position, displacement and occupancy parameters are given in Supplementary Table S5. The crystallographic information files have been deposited with the Principal Editor of *Mineralogical Magazine* and are available as Supplementary material (see below).

Selected bond distances derived from refinements using ionised-atom scattering factors are shown in Table 4 (Guo *et al.*, 2000a; Robinson *et al.*, 1971) (further details and atomic position coordinates and anisotropic displacement parameters are listed in Table S5). Here, O1 indicates oxygen linked with Si, whereas O2 indicates the oxygen shared by Si, Al and Be. Si–O has the shortest (1.61 Å) while Al–O has the longest bond length (1.91 Å).

The derived crystal structure is shown in Fig. 8a (projected onto (0001)) and Fig. 8b with its edge-linked distorted tetrahedrally coordinated T2 (Be) and octahedrally coordinated A (Al) sites. Crystal channels are characterised by the wide C1/2a site between the rings and narrow C2/2b site of the interior of the tetrahedral $[Si_6O_{18}]^{12-}$ ring with diameters of ~5.2 Å and ~2.6 Å, respectively. Figure 8c shows C2 site occupation with Na^+ and associated type IId, IIs and I water configurations, with the distinct coordination of two water molecules to Na^+ (type IId), one water molecule and optionally C1 site occupation with CO_2 (type IIs), or the alkali cation free-water configuration (type I) (Fridrichová *et al.*, 2016).
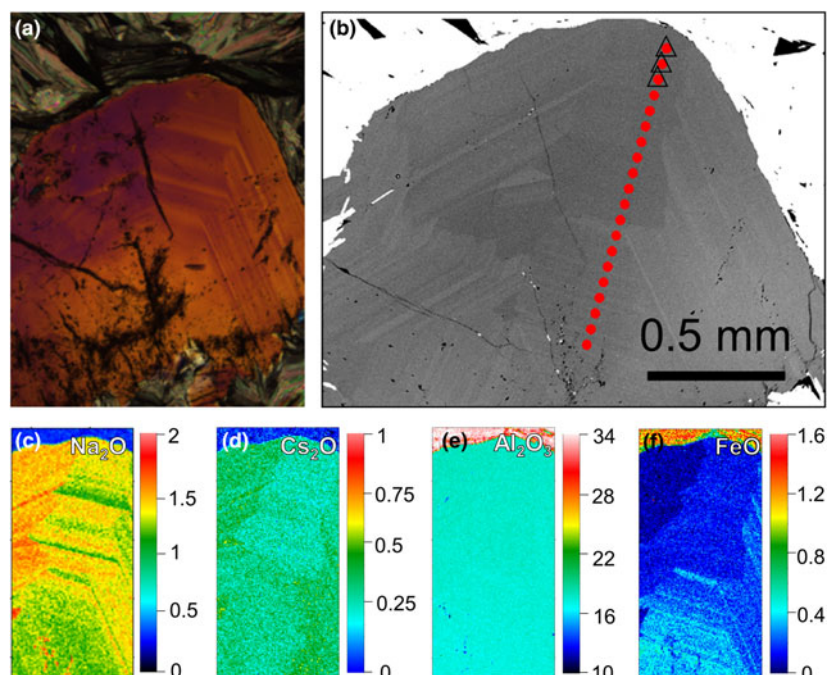
Fig. 6. Concentric zoning of beryl of thin section sample 1702B2 (green rectangle in Fig. 5a and 5b). (a) Optical microscope image under crossed polarisation; and (b) BSE image with EMPA transect (red dots), triangles indicate the selected EMPA points listed in Table 1. (c–f) Quantitative mapping of selected area for Na_2O, Cs_2O, Al_2O_3 and FeO, respectively (scale bar oxide wt.%).

Generally similar site occupancy values for the different lattice sites are found for all three crystals analysed. The A, T1 and T2 sites are almost fully occupied. The site population calculation is in good agreement with the EMPA and LA-ICP-MS data with a significant Li^+ substitution for Be^{2+} (T2) and minor M^{2+} substitution for Al^{3+} (A), charge balanced predominantly by Na^+ as the only alkali occupying the small C2 site, and the larger alkali (K^+, Cs^+, Rb^+) and $Fe^{2+/3+}$ together with water and minor CO_2 on the C1 site.

Raman spectroscopy

Representative polarisation-resolved Raman spectra, reflecting the different crystal orientations and type I and II water orientation, are shown in Fig. 9. Here, E_{inc} and E_R represent incident fundamental pump polarisation and Raman scattered polarisation, respectively. All spectra of different sample locations have negligible background indicating high structural integrity and overall low defect/inclusion density. The peaks below $1400\ cm^{-1}$ are associated with beryl lattice phonon modes (For Raman peak frequencies and mode assignment see Table S6 (Kim *et al.*, 1995; Qi *et al.*, 2001b). The strong peaks at $685\ cm^{-1}$ and $1066\ cm^{-1}$ are due to Si–O vibrations. The modes at $322\ cm^{-1}$ and $396\ cm^{-1}$ are Al–O bands. The two bands at $524\ cm^{-1}$ and $1009\ cm^{-1}$ represent Be–O vibrations. In the water stretch region the two and only partially resolved peaks are due to type II ($3594\ cm^{-1}$) and type I ($3604\ cm^{-1}$) water.

The non-degenerate symmetry modes (A_{1g}) which have the strongest Raman response are shown in Fig. 9a, b. The doubly degenerate symmetry modes (E_{1g}) are presented in Fig. 9c, d. The Raman emission of water, polarised perpendicular with respect to the c axis of beryl, is weak when the incident field is polarised parallel with respect to the c axis, as expected and shown in Fig. 9d. Doubly degenerate symmetric modes E_{2g} are presented in Fig. 9e, f, in which $398\ cm^{-1}$ and $684\ cm^{-1}$ are due to Si–O and Al–O vibrations, respectively, and with a corresponding water peak (Kim *et al.*, 1995; Hagemann *et al.*, 1990). The combination of Fig. 9b and 9f confirm the expected molecular orientation of type I and type IIs water (Hagemann *et al.*, 1990). Type I is expected to be more polarisable along the c axis, and thus stronger in Fig. 9b, while type II is expected to be more polarisable perpendicular with respect to the c axis and thus stronger in the polarisation combination of Fig. 9f, as observed. Polarised Raman spectra with the incident wave vector perpendicular with respect to the $(10\bar{1}0)$ face and unpolarised Raman spectra are shown in Fig. S4.

Micro-IR spectroscopy and mapping of water content

A representative IR point spectrum is shown in Fig. 10 from (a) transect #Q3-7 and (b) acquired parallel with respect to the LA-ICP-MS line on #Q3 in Fig. 7 (see also inset Fig. 10b). Infrared peak frequencies and mode assignments are listed in Table S2 (Charoy *et al.*, 1996; Qi *et al.*, 2001d; Łodziński *et al.*, 2005; Adamo *et al.*, 2008; Della Ventura *et al.*, 2015; Mashkovtsev *et al.*, 2016). The spectrally narrow bending (v_2^I) and asymmetric stretch (v_3^I) of type I (1600 and $3694\ cm^{-1}$), bending (v_2^{IIs}) and symmetric stretch (v_1^{IIs}) of type IIs water (1637 and $3588\ cm^{-1}$), and asymmetric CO_2 stretch ($2358\ cm^{-1}$) modes can be discerned. The broad peak at $\sim1950\ cm^{-1}$ has been assigned to the overtone absorption of a lattice phonon mode (Charoy *et al.*, 1996). The detailed transects for the type I and II stretch modes in Fig. 10b show an inversion in relative type I and II water content at the transition from primary to secondary beryl. Further, the type II peak is split as seen in the magnified region of Fig. 10c, with the main peak v_1^{IIs} at $\sim3588\ cm^{-1}$ corresponding to type IIs, and the shoulder at $\sim3605\ cm^{-1}$ corresponding probably to a combination of the symmetric stretches of type I (v_1^I) and type II water (v_1^{IId}). The minor peak at about $3651\ cm^{-1}$ is due to the antisymmetric stretch of type IIs water (v_3^{IIs}).

To determine relative peak intensities, the spectra have been fitted using simple Lorentzian lineshapes, with 5-6 peaks (dashed lines in Fig. 10c, see also supplement Fig. S5), with centre

Table 1. Quantitative elements content obtained by EMPA for thin sections (TS) and single crystals (SC)*

Sample number		#1702B2 TS	#1702B2 TS	#1702B2 TS	#1901 TS	#1901 TS	#Q7 SC	#Q7 SC
Wt.% oxide	Ideal crystal	Low-Na ○	High-Na □	Int.- Na △	High-Na ☆	Low-Na ◇	Low-Na	High-Na
Na_2O	-	1.231	1.690	1.338	2.005	1.130	1.422	1.719
MgO	-	0.193	0.026	0.025	0.033	0.064	0.179	0.001
K_2O	-	0.020	0.029	0.018	0.005	0.010	0.035	0.007
Cs_2O	-	0.416	0.481	0.315	0.152	0.389	0.486	0.093
CaO	-	0.004	0.016	0.005	-	0.001	-	-
TiO_2	-	0.032	-	0.005	-	0.010	-	0.004
FeO	-	0.495	0.067	0.139	0.013	0.235	0.170	-
MnO	-	0.026	-	0.005	0.000	0.021	-	-
SiO_2	67.07	64.668	64.479	64.507	64.360	64.841	64.705	64.914
Al_2O_3	18.97	17.810	18.307	18.210	18.481	18.366	18.079	18.516
Li_2O_{cal}		0.594	0.815	0.645	0.967	0.545	0.685	0.829
BeO_{cal}	13.96	12.481	12.088	12.365	11.827	12.628	12.336	12.150
Total	100.00	97.969	97.999	97.578	97.843	98.243	98.098	98.234
apfu								
Na	-	0.221	0.304	0.241	0.361	0.202	0.255	0.307
Mg	-	0.027	0.004	0.004	0.005	0.009	0.025	0.000
K	-	0.002	0.003	0.002	0.001	0.001	0.004	0.001
Cs	-	0.016	0.019	0.012	0.006	0.015	0.019	0.004
Ca	-	0.000	0.002	0.001	0.000	0.000	-	-
Ti	-	0.002	0.000	0.000	0.000	0.001	-	0.000
Fe	-	0.034	0.005	0.010	0.001	0.016	0.012	-
Mn	-	0.002	-	0.000	0.000	0.002	0.000	-
Si	6	5.994	5.986	5.992	5.978	5.980	5.993	5.989
Al	2	1.945	2.003	1.993	2.023	1.996	1.973	2.013
Li_{fixed}		0.221	0.304	0.241	0.361	0.202	0.255	0.307
Be_{cal}	3	2.779	2.696	2.759	2.639	2.798	2.745	2.693

*Every value represents the average of three analyses. The measured points for ○ and □ are shown in Fig. 5, △ is shown in Fig. 6, ☆ and ◇ are shown in Fig. S2. –: close or below the detection limit.

Li_{fixed}: Li set to the Na value based on correlation derived from LA-ICP-MS; 'cal': calculated value, $Be_{cal} = 3 - Li$.
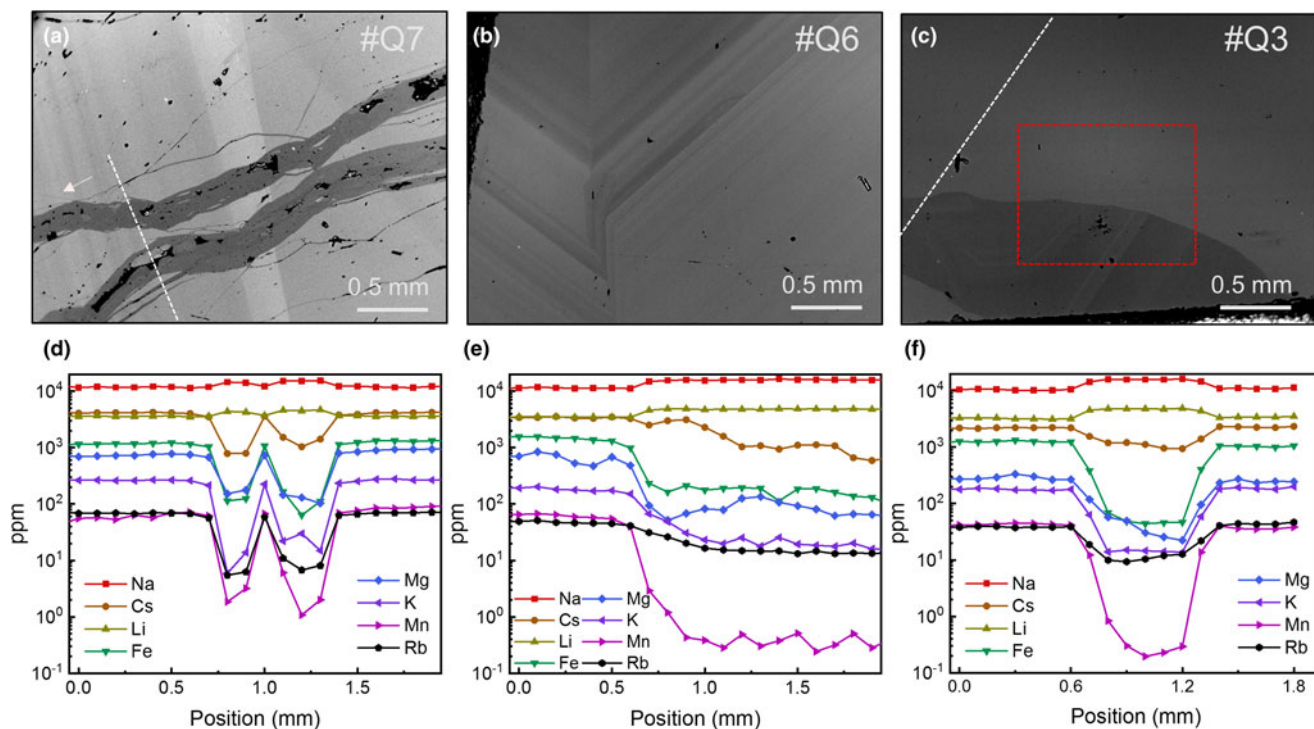

Fig. 7. Representative BSE images of single crystal samples #Q7 (a), #Q6 (b) and #Q3 (c), with LA-ICP-MS transects (d–f, dashed lines in (a) and (c)): transect (d) location is ~0.3 mm just left of field of view in (a) at extension of meandering secondary feature. Transect (e) is not related to (b) with location indicated in Fig. 3b. Transect (f) shown in (c) as indicated, the full position is shown in inset of Fig. 10b. The LA-ICP-MS elemental pattern reflects primary and secondary beryl phases, with characteristic positive correlation of Na and Li, both negatively correlated with all other trace elements. Area in (c) (red dashed rectangle) indicates micro-IR mapping #Q3-2 as shown in Fig. 12.

Table 2. Representative minor- and trace-element composition of beryl determined by LA-ICP-MS.*

ppm	#Q7-3 S	#Q7-3 P	#Q6-1 S	#Q6-1 P	#Q3-1 S	#Q3-1 P
Li	4611.20	3498.59	4462.00	3433.05	4732.43	3264.07
Na	15,179.02	11,414.04	15,069.01	11,269.89	15,795.65	10,484.95
Mg	145.29	750.37	327.22	720.82	25.57	293.78
P	27.76	16.01	28.83	11.66	14.79	15.90
S	73.57	66.73	50.84	54.80	44.67	47.49
K	22.02	260.59	37.25	194.15	14.09	183.23
Ca	18.60	53.72	16.46	70.35	21.92	75.41
Ti	35.68	20.70	20.02	3.36	5.92	11.15
Mn	6.02	71.22	0.21	66.12	0.23	39.11
Fe	165.55	1157.46	40.43	1550.04	45.93	1167.36
Zn	6.74	54.53	1.17	49.13	13.28	58.39
Ga	11.82	29.84	15.52	14.90	29.69	10.88
Rb	10.92	67.63	11.16	49.83	11.96	37.98
Cs	1520.71	4019.28	870.63	3170.35	958.81	2080.47
Apfu						
Li	0.3589	0.2723	0.3473	0.2672	0.3683	0.2540
Na	0.3566	0.2682	0.3540	0.2648	0.3711	0.2463
Mg	0.0032	0.0167	0.0073	0.0160	0.0006	0.0065
P	0.0005	0.0003	0.0005	0.0002	0.0003	0.0003
S	0.0012	0.0011	0.0009	0.0009	0.0008	0.0008
K	0.0003	0.0036	0.0005	0.0027	0.0002	0.0025
Ca	0.0003	0.0007	0.0002	0.0009	0.0003	0.0010
Ti	0.0004	0.0002	0.0002	0.0000	0.0001	0.0001
Mn	0.0001	0.0007	0.0000	0.0007	0.0000	0.0004
Fe	0.0016	0.0112	0.0004	0.0150	0.0004	0.0113
Zn	0.0001	0.0005	0.0000	0.0004	0.0001	0.0005
Ga	0.0001	0.0002	0.0001	0.0001	0.0002	0.0001
Rb	0.0001	0.0004	0.0001	0.0003	0.0001	0.0002
Cs	0.0062	0.0163	0.0035	0.0129	0.0039	0.0085

*S indicates the secondary phase of beryl while P indicates the primary phase.

Table 3. Crystal structure refinement parameters for beryl from Xuebaoding (#Q7, #Q6, and #Q3) compared to reported data.

	#Q7	#Q6	#Q3	Reported data[a]
a (Å)	9.2161(2)[b]	9.2162(2)[b]	9.2171(4)[b]	9.209(2)
c (Å)	9.2178(2)[b]	9.2182(2)[b]	9.2219(4)[b]	9.2221(9)
V (Å³)	678.03(3)	678.08(3)	678.48(7)	677.4(2)
Space group	$P6/mcc$	$P6/mcc$	$P6/mcc$	$P6/mcc$
Z	2	2	2	2
Radiation	Mo$K\alpha$	Mo$K\alpha$	Mo$K\alpha$	Mo$K\alpha$
2θ range (°)	0–80.77	0–80.59	0–80.76	5.1–49.98
Reflections measured	41515	77872	77620	-
Unique reflections	767	762	767	775
$R(\sigma)$	0.0104	0.0099	0.0130	-
R_{int}	0.0384	0.0350	0.0395	0.0352
R_1	0.0249[c]	0.0268[c]	0.0295[c]	0.0371

[a]Guo *et al.* (2000).
[b]Unit cell refinement obtained from point detector data.
[c]Using ionised atom scattering factors for cations (Cromer and Mann, 1968) and for O²⁻ (Azavant and Lichanot, 1993).

Table 4. Selected interatomic distances (Å) for beryl from Xubaoding in comparison to reported data.

	#Q7	#Q6	#Q3	Reported data[a]
Be tetrahedron (T2)				
Be–O2 (4)	1.6656(6)	1.6659(8)	1.6655(7)	1.6722(5)
Polyhedral volume (Å³)	2.0811	2.0825	2.0790	-
Quadratic elongation[b]	1.0909	1.0908	1.0915	-
Al octahedron (A)				
Al–O2 (6)	1.9094(6)	1.9097(7)	1.9095(6)	1.9065(6)
Polyhedral volume (Å³)	9.0066	9.0111	9.0092	-
Quadratic elongation	1.0202	1.0202	1.0202	-
Si tetrahedron (T1)				
Si–O1	1.6017(8)	1.6021(10)	1.6010(9)	1.5985(7)
Si–O1	1.6044(8)	1.6046(10)	1.6049(9)	1.6054(6)
Si–O2 (2)	1.6153(6)	1.6149(7)	1.6164(7)	1.6118(5)
Average Si–O	1.6092	1.6092	1.6097	1.6052
Polyhedral volume (Å³)	2.1337	2.1334	2.1359	-
Quadratic elongation	1.0015	1.0016	1.0015	-
Na channel (C2)				
Na–water (2)	2.3044(0)	2.3045(0)	2.3055(1)	-
Na–O1 (6)	2.5561(10)	2.5547(12)	2.5577(11)	2.553(0)
Polyhedral volume (Å³)	26.078	26.050	26.1223	-

[a]Guo *et al.* (2000); [b] Robinson *et al.* (1971)

frequencies of ν_1^{IIs} and ν_3^{I} of 3588 cm⁻¹ and 3694 cm⁻¹, respectively. The frequencies vary by less than ±1 cm⁻¹ between primary and secondary crystal phases.

The spatial variation of the relative IR peak absorption for type I and IIs water and CO_2 across the primary and secondary phase is shown in Fig. 11a. The increase in spectral intensity of ν_1^{IIs} (orange) is observed in the secondary phase (1.0 to 1.7 mm), while ν_3^{I} (brown) decreases. The mixed shoulder at ~3605 cm⁻¹ (black) correlates with the ν_3^{I} intensity, suggesting that it is associated primarily with ν_1^{I}. Additionally, the CO_2 stretch (purple) slightly decreases in the secondary phase.

The corresponding absolute amount of water can be estimated based on the Lambert–Beer law $A = \varepsilon c d$, where A is the absorbance, ε the molar absorption coefficient (L/mol·cm), c the water concentration (mol/L), and d the sample thickness (cm) (Fukuda *et al.*, 2009). In our case, the sample thickness of #Q3 is ~120 μm. We use reported molar absorption coefficients of type I (3696 cm⁻¹) and type IIs (3588 cm⁻¹) water modes of $\varepsilon_I = 197$ L/mol·cm
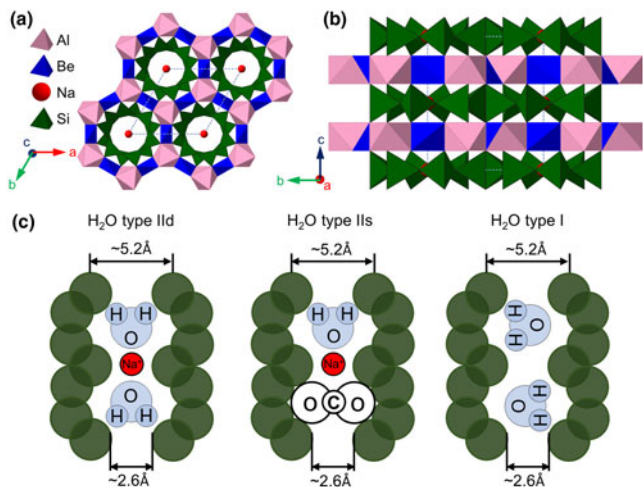
Fig. 8. Crystal structure of beryl. (a) Along orientation parallel with respect to the *c* axis; (b) perpendicular with respect to the *c* axis, with octahedral A (Al), tetrahedral T2 (Be), Si, and two channel sites at the C1/2a (H_2O, large alkali) and C2/2b (Na) positions; and (c) type IId, type IIs and type I H_2O molecule configuration, with corresponding Na^+ and CO_2 positions on channel sites (after Fridrichová *et al.*, 2016).

of beryl calculated from XRD of $\rho = 2.75$ g/cm^3, with its variation with Na^+ content negligible for our case, the amount of water can be obtained as H_2O_{tot} (wt.%) $= c \times M \times 10^{-1}/\rho$ where M is the molar mass of water. An ideal and maximum 1 apfu water on C1 corresponds to 3.24 wt.% for an ideal beryl with $M = 537.47$ g/mol (Hawthorne and Černý, 1977; Pankrath and Langer, 2002).

The resulting apfu values based on the Lambert–Beer law for ν_1^{IIs} and ν_3^I from Fig. 11a and their sum are shown in Fig. 11b. Type IIs water (orange) increases from 0.20 apfu in the primary phase to 0.38 apfu in the secondary phase, correlates positively with Na^+ (red), and correlates negatively with Fe^{3+} (green) based on the co-localised LA-ICP-MS transect. Meanwhile, type I water (brown) decreases from 0.21 apfu in the primary phase to 0.12 apfu in the secondary phase. It appears that the ~50% decrease of type I water in the secondary zone is more than compensated by a corresponding increase in type IIs water, with the total water content ($\nu_1^{IIs} + \nu_3^I$) (blue) increasing from 0.42 apfu in the primary phase to 0.50 apfu in secondary beryl.

The amount of water of 0.42 apfu determined for the primary phase by IR absorption is in good agreement with the value of 0.40 apfu derived from XRD (Table 5). The XRD result further suggests that the C1 site is almost half occupied with a combination of the trace amounts of alkali K^+, Cs^+ and Rb^+, together with water (see Table 5). The approximately equal total amount of water in primary and secondary beryl is interesting to note, with primarily a change in ratio of type I to type II water, which is controlled by the different Na^+ content (occupying the C2 site).

Corresponding spatial images are shown in Fig. 12 of type I water (a, d), type II water (b, e) and CO_2 (c, f) peak integrated
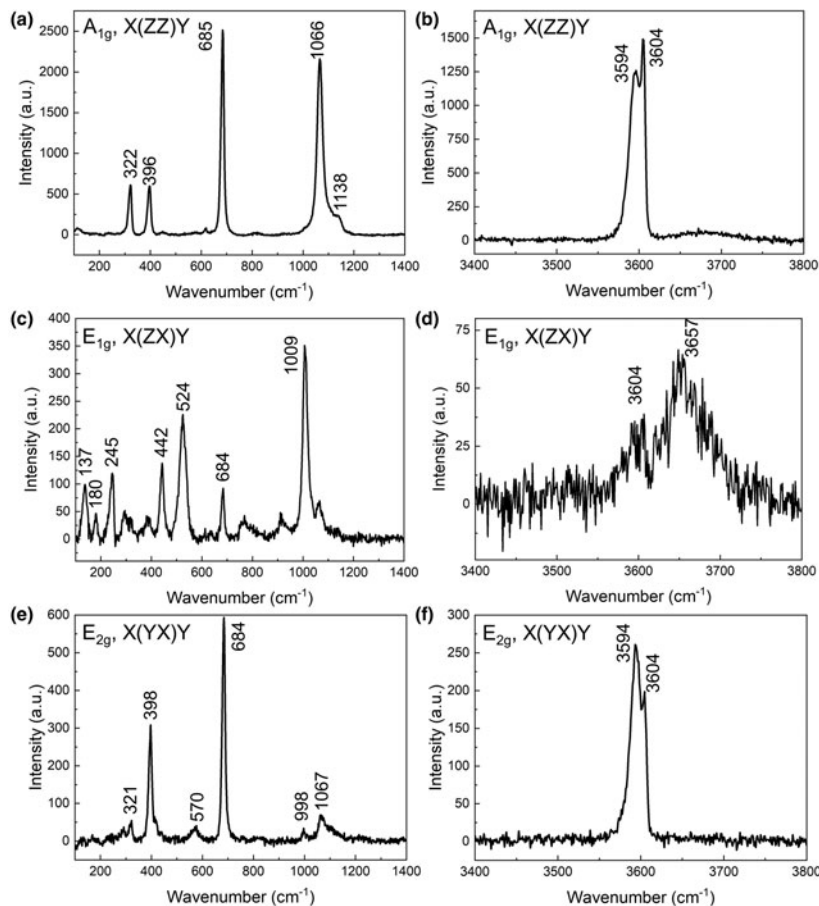
(Charoy *et al.*, 1996), and $\varepsilon_{IIs} = 256$ L/mol·cm, respectively (Goldman *et al.*, 1977). Though the value for ε_{IIs} is for cordierite, we expect it to equally apply for beryl to a good approximation given the similarity in water structure and index of refraction in the IR. Absorption peak intensity A for each mode is approximated by the ratio of fitted peak area and line width. Using a density value

Fig. 9. Polarised Raman spectra of beryl. (a,b) k ⊥ *c* axis and E_{inc} // *c* axis and E_R // *c* axis, (c,d) k ⊥ *c* axis and E_{inc} // *c* axis and E_R ⊥ *c* axis, (e,f) k ⊥ *c* axis and E_{inc} ⊥ *c* axis and E_R ⊥ *c* axis. k is the incident wave-vector, E_{inc} and E_R are the polarisation directions of the fundamental and Raman light, respectively. The crystallographic *z* axis is parallel to optical *c* axis. A_{1g} indicates the non-degenerate symmetric modes, E_{1g} / E_{2g} indicate the doubly degenerate symmetric modes. Peak assignments are listed in Table S6.
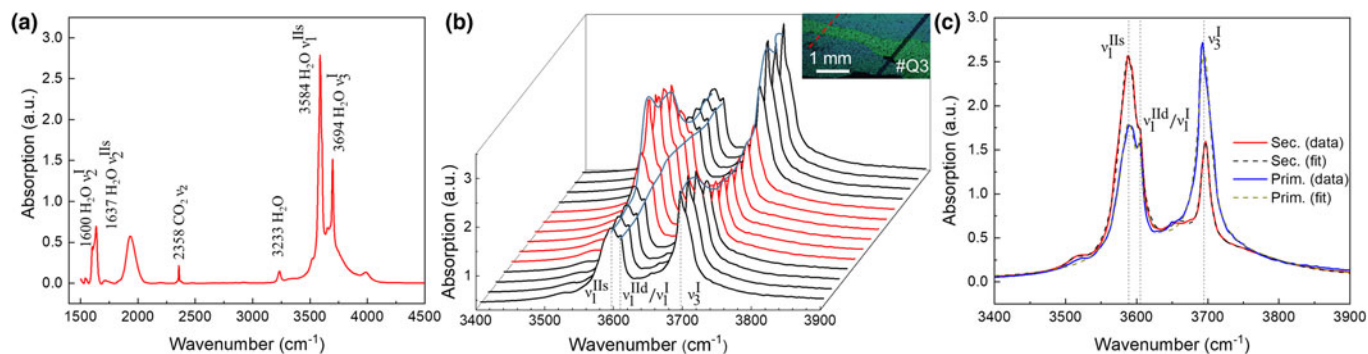
Fig. 10. IR point spectrum and micro-IR transect #Q3-7 (for location see Fig. 3c). (a) Peak assignment with type I water (1600 and 3694 cm^{-1}), type II water (1637 and 3584 cm^{-1}) and CO$_2$ (2358 cm^{-1}). (b) IR spectral transect with spectra centred on the water stretch region crossing secondary beryl zone (red) with primary beryl on either side (black) (inset: optical micrograph, with IR transect in red and LA-ICP-MS line in black). (c) Representative spectra from primary (blue) and secondary (red) zone with intense negative correlation of type I and type II water, with Lorentzian line fits (dashed) for type IIs (3588 cm^{-1}), mixed type IId/I (3605 cm^{-1}) and type I (3694 cm^{-1}) (for details see also Fig. S5).
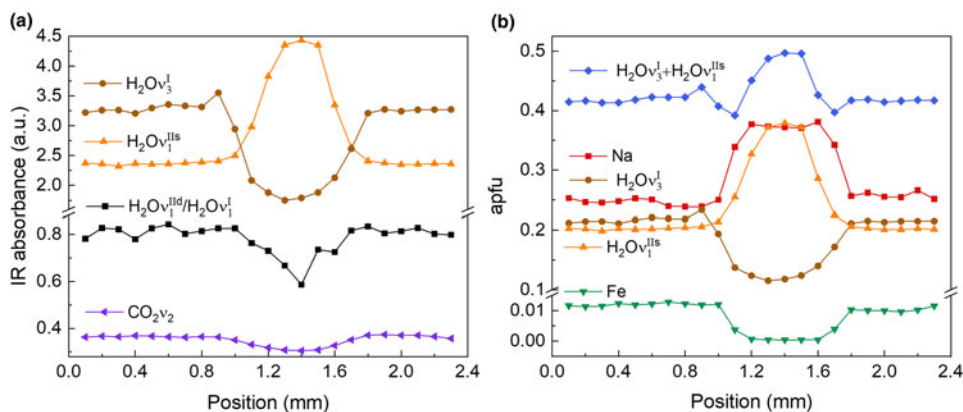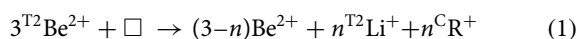

Fig. 11. IR and ICPMS transect analysis of #Q3-7 (see Fig. 3c and Fig. 7c). (a) IR-absorbance from Lorentzian peak fits showing qualitative correlated and anti-correlated variations of CO$_2$, type I and IIs water across primary and secondary zones. (b) Quantitative comparison of type I and type IIs (type IId negligible) water (apfu) derived from absolute IR absorption cross sections, in relation to Na and Fe content from LA-ICP-MS.

values for the two crystal regions #Q3-2 (a–c) and #Q3-9 (d–f) as indicated in Fig. 3c and acquired in proximity and an either side of the LA-ICP-MS trace (images of minor band centred at 3605 cm^{-1} is shown in Fig. S6 and full width at half maximum of type I in S7). Akin to the IR line trace analysis above, the same negative correlation of type I and type II water, and positive correlation of type I water with CO$_2$ stand out.
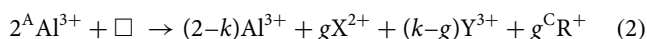
Discussion

Coupled substitution

In the following we analyse the role of the two primary substitution vectors for the octahedrally coordinated A and tetrahedrally coordinated T2 site (Belov, 1958; Wood and Nassau, 1968; Bakakin *et al.*, 1969; Hawthorne and Černý, 1977; Aurisicchio *et al.*, 1988; Sherriff *et al.*, 1991) with

$$3^{T2}Be^{2+} + \square \rightarrow (3-n)Be^{2+} + n^{T2}Li^+ + n^C R^+ \quad (1)$$

and

$$2^A Al^{3+} + \square \rightarrow (2-k)Al^{3+} + gX^{2+} + (k-g)Y^{3+} + g^C R^+ \quad (2)$$

where R$^+$ represent alkali ions, X^{2+} the divalent cations, Y^{3+} trivalent cations, with respective coefficients *n, k,* and *g.*

Summarising the data from all EMPA and LA-ICP-MS in Fig. 13 shows the corresponding correlations for A and T2 site substitution and indicates only a weak coupling between the two substitution vectors.

Figure 13a shows the negative correlation of 2$^+$/3$^+$ cations with Al^{3+} content based on sets of EMPA values from different samples (#Q3, #Q6 and #Q7), in comparison with the theoretical behaviour based on equation 2 with slope –1. Here we assume that all Fe^{2+}/Fe^{3+} ions occupy the A site. The small deviation of the data from the ideal behaviour is probably due to slightly too high Al EMPA values, as supported by XRD suggesting Al < 2 apfu, or that Fe is dominated by Fe^{3+} (see also below). Overall, the role of A-site substitution is small, with the sum of divalent trace elements ranging from as low as ~0.001 apfu to a maximum value not exceeding ~0.06 apfu.

Figure 13b shows the positive correlation of Na$^+$ with Li$^+$ closely following the ideal behaviour with slope 1. This shows that the substitution vector equation 1 is dominated by Na$^+$ alone, which ranges from 91.5%–99.7% (apfu) of the sum of all alkali elements, and charge balancing for Li$^+$ as it substitutes for Be^{2+}. This suggests that the remaining alkalis K$^+$, Rb$^+$ and Cs$^+$ are primarily charge balancing the Al^{3+} substitution for divalent cations at the A site. Note the bimodal distribution with lower Li$^+$ and Na$^+$ content in the primary, and higher Li$^+$ and Na$^+$ values in the secondary phases. Correspondingly this behaviour is to first order inversed for the other alkalis *vs.* X^{2+} cations (Fig. 13c). This suggests that in the secondary phase the role of

Fig. 12. Micro-IR imaging on primary and secondary beryl of #Q3-2 (a–c) and #Q3-9 (d–f) (area indicated in Figs 3c, 7c), based on peak intensities of (a and d) type I water (3694 cm^{-1}), (b and e) type IIs water (3584 cm^{-1}) and (c and f) CO$_2$ (2358 cm^{-1}). Type I water is less (blue area in (a and d)), while type IIs water is more in the secondary phases (red area in (b and e)). CO$_2$ (c and f) correlates with type I water.
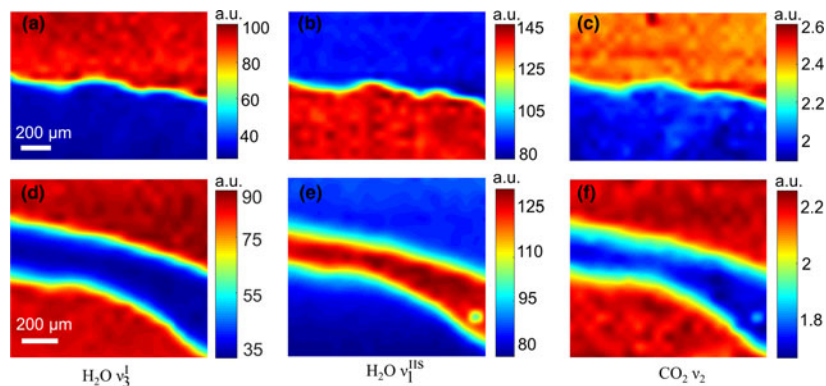
Table 5. Site-scattering refinement with site scattering and site population assignment from single crystals #Q7, #Q6 and #Q3, compared to the results of EMPA and LA-ICP-MS analysis.

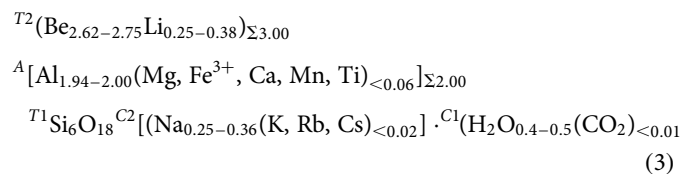| Crystal sample	Site	Site scattering from refinement (epfu)	Site population assignment (apfu)	Site population (from average chemical composition from EMP and ICP-MS) (apfu)	Predicted site scattering from chemical composition (epfu)
#Q7	T2	5.90(12)	2.95(6) Be^{2+}	0.289 Li$^+$ + 2.711 Be^{2+}	6
	A	19.94(11)	1.994(1) Al^{3+}	1.973 Al^{3+} + 0.022 Mg^{2+} + 0.008 Fe^{3+}	20.13
	T1	59.64(2)	5.964(2) Si^{4+}	5.998 Si^{4+}	59.98
	C2	3.096(2)	0.3096(2) Na$^+$	0.293 Na$^+$	2.93
	C1	4.56(2)	0.456(2) H$_2$O	0.003 K$^+$ + 0.015 Cs$^+$ + 0.368 H$_2$O*	4.56
#Q6	T2	5.81(12)	2.905(6) Be^{2+}	0.284 Li$^+$ + 2.716 Be^{2+}	6
	A	19.86(13)	1.986(1) Al^{3+}	2.020 Al^{3+} + 0.010 Mg^{2+} + 0.009 Fe^{3+}	20.51
	T1	60.00(4)	6.0(4) Si^{4+}	5.969 Si^{4+}	59.69
	C2	3.2244(2)	0.32244(2) Na$^+$	0.358 Na$^+$	3.58
	C1	4.86(2)	0.486(2) H$_2$O	0.004 Cs$^+$ + 0.464 H$_2$O*	4.86
#Q3	T2	5.83(12)	2.915(6) Be^{2+}	0.249 Li$^+$ + 2.751 Be^{2+}	6
	A	19.89(12)	1.989(1) Al^{3+}	2.008 Al^{3+} + 0.003 Mg^{2+} + 0.009 Fe^{3+}	20.32
	T1	59.88(2)	5.988(2) Si^{4+}	5.982 Si^{4+}	59.82
	C2	2.928(2)	0.2928(2) Na$^+$	0.252 Na$^+$	2.52
	C1	4.56(2)	0.456(2) H$_2$O	0.003 K$^+$ + 0.009 Cs$^+$ + 0.401 H$_2$O*	4.56

epfu – electrons per formula unit
H$_2$O* is estimated by site scattering (epfu) except sum of K$^+$, Cs$^+$ and Rb$^+$.

the T2 substitution vector (equation 1) increases, whereas the A substitution vector (equation 2) diminishes. The deviations of certain data groups (green and red) in Fig. 13c with negative correlation in Fig. 13b suggests a weak coupling between the two substitution vectors through the alkali R$^+$ mixing.

Combining both substitutions of equations 1 and 2 in Fig. 13d shows the sum of the vector Li$^+$ for Be^{2+} at the T2 site, and the sum of all divalent cations to replace for Al^{3+} at the A site. The good agreement with the theoretical slope of 1 for all data, in contrast to (b) or (c) suggests that all iron at the A site is trivalent, i.e. not necessitating charge balancing with alkalis (Fe with other divalent cations *vs.* alkali elements see Fig. S8).

The combined results can then be expressed by the empirical formula:

$$^{T2}(\mathrm{Be}_{2.62-2.75}\mathrm{Li}_{0.25-0.38})_{\Sigma 3.00}$$

$$^{A}[\mathrm{Al}_{1.94-2.00}(\mathrm{Mg, Fe}^{3+}, \mathrm{Ca, Mn, Ti})_{<0.06}]_{\Sigma 2.00}$$

$$^{T1}\mathrm{Si}_6\mathrm{O}_{18}{}^{C2}[(\mathrm{Na}_{0.25-0.36}(\mathrm{K, Rb, Cs})_{<0.02}]\cdot{}^{C1}(\mathrm{H}_2\mathrm{O}_{0.4-0.5}(\mathrm{CO}_2)_{<0.01}$$

$$(3)$$

In accordance with the International Mineralogical Association Commission on New Minerals, Nomenclature and Classification guidance (Bosi *et al.*, 2019), this formula leads to the end-member composition $^{T2}\mathrm{Be}_3{}^{A}\mathrm{Al}_2{}^{T1}\mathrm{Si}_6\mathrm{O}_{18}$ (beryl). In summary, the sample studied can be classified as (Li, Na-rich) beryl.

Crystal structure

The Si value close to ideal 6 apfu by EMPA indicates a negligible Si–Al substitution. The tetrahedral volumes are 2.133, 2.133 and 2.136 Å^3 for #Q7, #Q6 and #Q3 (Table 4), respectively, values typical for pure Si tetrahedral sites.

The distinct coordination of water with Na$^+$ features a shorter bond length of H–O1 for type IIs compared to type IId (Fukuda and Shinoda, 2008, 2011). This results in a correspondingly larger bond strength giving rise to a higher frequency of the IR bending mode. Our type IIs bending mode value of 1637 cm^{-1} agrees with the range of theoretical peak positions of 1637–1639 cm^{-1} for type IIs water rather than 1624–1627 cm^{-1} for type IId water (Fridrichová *et al.*, 2016).

Theoretical Na–O bond lengths of type IIs and IId are 2.227 Å and 2.483 Å, and Na–O1 bond lengths of IIs and IId are 2.558 Å and 2.540 Å, respectively (Fridrichová *et al.*, 2016). The IIs values are in good agreement with our measured values of the average Na–O and Na–O1 band lengths of 2.305 Å and 2.556 Å, respectively. This indicates the Na bound water is primarily type IIs.
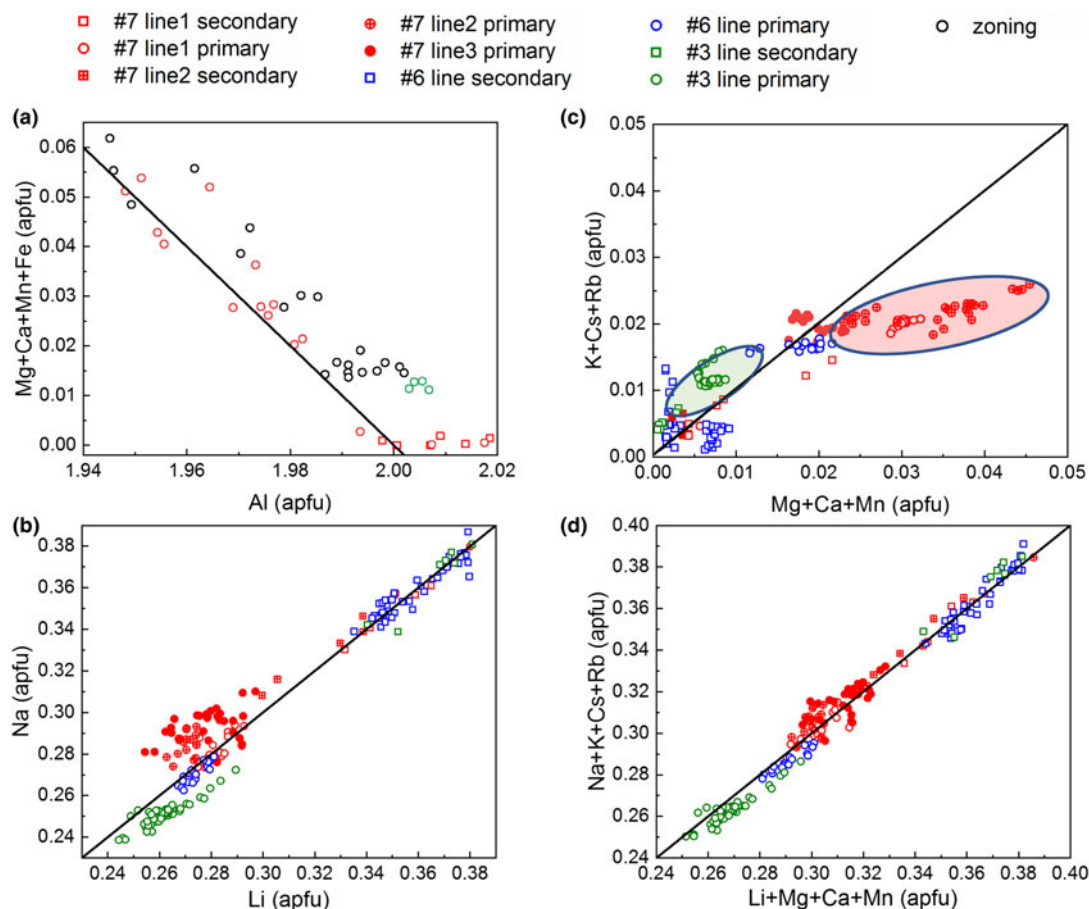
Fig. 13. Correlations and trends in major-element variations. (a) Linear correlation between A-site Al and corresponding X^{2+} (divalent ions at the A site) substituents. (b) Correlation between T2 Li^+ substitution for Be^{2+} with Na^+ charge balancing on the C2 site. (c) $R^+ - Na^+$ vs. X^{2+} with inversely correlated deviations of some data groups compared to (b), indicating weak coupling between the two substitution vectors. (d) Combined A and T2 substitution expressed as R^+ (monovalent alkali ions in channel) vs. $Li^+ + X^{2+} - Fe^{3+}$ with linear correlation. (a) Based on microprobe, (b–d) LA-ICP-MS data. Black lines represent the ideal substitution or charge balance relationship, $Al^{3+} + X^{2+} = 2$ (a); $Li^+ = Na^+$ (b); $R^+ - Na^+ = X^{2+}$ (c) and $R^+ = Li^+ + X^{2+} - Fe^{3+}$ (d).

Water content

The water estimates based on the absolute IR absorbed intensity, consistent with the results from XRD informed by LA-ICP-MS, indicate that the water occupancy ranges from 0.4 apfu to 0.5 apfu in #Q7, which is close to half of the maximum water occupation with an approximate stoichiometry of $Be_3Al_2Si_6O_{18}\cdot 0.5H_2O$. Similarly, from XRD, the water occupation is close to 0.5 apfu for #Q6 (0.46), yet slightly low for #Q7 (0.37) and #Q3 (0.40). The Na^+ content (C2/2b site) controls the dipole orientation and types of water on the channel site in the centre of the Si rings (C1/2a site) with type II water correlated with Na^+ content as expected.

Few other investigations have yet addressed the water content in Xuebaoding beryl. Only Guo *et al.* (2000b) and Lin *et al.* (2000) have estimated the water content using a wet chemical method and obtained values of 1.97 wt.% to 3.56 wt.% corresponding to apfu values ranging from 0.61 to 1.13, with the later value exceeding the maximum possible value of 1 apfu.

From other localities, water content in beryl was determined by wet-chemical analyses (Charoy *et al.*, 1996; Guo *et al.*, 2000b; Lin *et al.*, 2000), thermogravimetric analyses (Artioli *et al.*, 1993; Pankrath and Langer, 2002; Gatta *et al.*, 2006; Fridrichová *et al.*, 2016), or based on the empirical equation

H_2O (in wt.%) = $[0.84958 \times Na_2O$ (in wt.%)] $+ 0.8373$ (Giuliani *et al.*, 1997; Groat *et al.*, 2008; Fridrichová *et al.*, 2016), with values ranging from <1 wt.% to >3 wt.%. However, these methods configure sensitivity to the type of water, or may overestimate including fluid inclusions or water on grain boundaries. This highlights the value of quantitative micro-IR spectroscopy with spatial resolution and site specificity.

Comparison with previous Xuebaoding beryl studies

The results of EMPA and LA-ICP-MS are in agreement with some but not all prior studies of beryl from Xuebaoding which are summarised in Table S1 and S7. In general good agreement is found with Guo *et al.* (2000b), Qi *et al.* (2001b) and Zhou *et al.* (2002). Yet results from Liu *et al.* (2001b), republished in Liu *et al.* (2005) are inconsistent with ours, reporting high SiO_2 (66.04–67.25 wt.%) and low Na_2O (0.42–0.83 wt.%). A bulk wet-chemical analysis (Liu *et al.*, 2001a; Qi *et al.*, 2001c) republished in Liu *et al.* (2005) and again in Liu *et al.* (2007) is in general agreement with our results, except for their third set of data with low Na_2O (0.27 wt.%) and high FeO^T (0.76 wt.%) (bolded data in Table S7). A later analysis by the same authors using LA-ICP-MS and XRF (Liu *et al.*, 2012) is again inconsistent

with implausibly high Li^+ (Li_2O 2.60–3.04 wt.%) that cannot be charge balanced by the other alkali as quantified. A single wet-chemical analysis (Lin *et al.*, 2000) reports exceptionally high Fe (0.67 wt.%) and Ca (0.88 wt.%).

Our XRD unit-cell parameter derived data are in good agreement with an earlier analysis of Guo *et al.* (2000a) with $a = 9.209(2)$ Å and $c = 9.2221(9)$ Å with $c/a = 1.0001$. However, our results are in disagreement with Liu *et al.* (2007) that reports implausibly short a and c values based on small number of reflections and poor R value. Instead, our results are in better agreement with earlier (Liu *et al.*, 2005) and later work (Liu *et al.*, 2012) by the same authors.

Comparison with beryl of similar structure and chemistry from other localities

The Xuebaoding beryl is overall characterised by a simple chemistry with minor octahedral (A) site substitution with Fe^{3+} and Mg^{2+} and negligible Ti^{4+}, Zn^{2+} or Ca^{2+} with charge balance through Cs^+ and minor Rb^+ and K^+. Fe as Fe^{3+} is suggested to substitute for Al^{3+} on the A site (Aurisicchio *et al.*, 1988; Neiva and Neiva, 2005; Groat *et al.*, 2008, 2010). The low Fe^{3+} content is consistent with only a light colour trend towards blue (aquamarine) (Mihalynuk and Lett, 2003; Fridrichová *et al.*, 2015; Lum *et al.*, 2016). Appreciable Li^+ substitution for Be^{2+} on the tetrahedral (T2) site with Li^+ up to 0.38 is on the high end compared to other localities worldwide (Aurisicchio *et al.*, 1988) and charge balanced by Na^+ incorporation on the channel site. This classifies the Xuebaoding beryl as '(Na, Li) beryl' (Černý, 1975) as typically associated with Li-rich pegmatites, and of the crystallographic 'tetrahedral' variety, i.e. the dominance of the T2 site Li substitution as opposed to A-site substitution (Aurisicchio *et al.*, 1988).

Compared to beryl from other localities worldwide, the chemical composition and structure of beryl from Xuebaoding do not stand out in any particular way (Hawthorne and Černý, 1977; Aurisicchio *et al.*, 1988, 1994; Sherriff *et al.*, 1991; Artioli *et al.*, 1993; Černý *et al.*, 2003; Groat *et al.*, 2008; Lum *et al.*, 2016). The Si^{4+} content of most beryl is close to 6. Al^{3+} apfu values generally range from as low as 1.2 in few cases, to 2, with the majority of data above 1.5 apfu, compared to Xuebaoding beryl with Al^{3+} close to 2 apfu. Be^{2+} ranges from 2.5 to 3.0 apfu (Hawthorne and Černý, 1977; Aurisicchio *et al.*, 1988, 1994; Sherriff *et al.*, 1991; Artioli *et al.*, 1993; Černý *et al.*, 2003), similar to Xuebaoding beryl varying between 2.62 and 2.75 apfu. Be^{2+} substitution for Li^+ and correlated with Na^+ is observed frequently with Li^+ ranging from 0 to 0.5 apfu (with Xuebaoding Li^+ of 0.25 to 0.4 apfu in the middle of that range).

With site substitution controlling the unit-cell parameters (Pankrath and Langer, 2002), the values for the a axis range from 9.202 to 9.228 Å and the c axis from 9.185 to 9.240 Å (Hawthorne and Černý, 1977; Aurisicchio *et al.*, 1988; Sherriff *et al.*, 1991; Artioli *et al.*, 1993; Černý *et al.*, 2003). Corresponding values for Xuebaoding beryl fall within the middle of that range. Notably similar in composition and unit-cell parameter to Xuebaoding beryl #Q7, is beryl from the Mount Bity region, Madagascar (pale pink sample #18, Aurisicchio *et al.*, 1988), with $Si^{4+} = 6$ and $Al^{3+} = 2$; $Li^+ = 0.27$ substituting Be^{2+} at the T2 site; and $Na^+ = 0.18$ and $Cs^+ = 0.02$ occupying the channel to balance the charge – resulting in $a = 9.215$ Å and $c = 9.218$ Å, closely resembling the Xuebaoding beryl values of $a = 9.2161(2)$ Å and $c = 9.2178(2)$ Å. The beryl from Pala, California, USA (pale pink sample #28, Aurisicchio *et al.*, 1988) with $a = 9.213$ Å

and $c = 9.212$ Å, and with similar composition of $Si^{4+} = 5.996$, $Al^{3+} = 2.004$, but lower $Li^+ = 0.17$ and $Na^+ = 0.14$ matches Xuebaoding sample #Q7 closely.

Comparison with tabular beryl worldwide

A particular feature of Xuebaoding beryl is the tabular habit. Similar tabular habits are observed in 'morganite' (pink beryl) (Cook, 2011) from San Diego County, California, USA, yet crystals exhibit dominance of A-site substitution (Mn^{2+}) with charge balanced by Cs^+ (on C1) and low water content. Clear beryl (goshinite) from lithium-rich microcline–albite pegmatites from Minas Gerais, Brazil (Cook, 2011) sometimes occur as tabular crystals, with high Li^+ and Na^+ content and are water rich (Fukuda and Shinoda, 2011). Similarly, tabular beryl from the Bikita rare-element granitic pegmatite, Zimbabwe, exhibit high Li^+ content and T2-site substitution (Černý *et al.*, 2003) with alkali charge balancing, and only minor A-site substitution. The beryl-group member pezzottaite with maximum lithium substitution on T2 (ideally $Cs(Be_2Li)Al_2Si_6O_{18}$, Yakubovich *et al.*, 2009) also exhibits a tabular habit. The crystal chemistry of the Xuebaoding beryl, while not deterministic with regards to the crystal habit, may still give some insight into the evolution of the ore-forming fluids (Černý, 2002; Černý *et al.*, 2003; Uher *et al.*, 2010; Sardi and Heimann, 2014). The alkali and ferromagnesian content can reflect the evolution and composition of the host fluid (Černý, 1975).

Summary and implications

Overall, the Xuebaoding beryl exhibit very similar tabular habit throughout the deposit, only rarely columnar, or etched. This suggests generally similar and stable conditions during the crystallisation of the veins. The low Fe^{3+} and Mg^{2+} content is consistent with the low degree of Fe^{3+} mineralisation in general (minor pyrite). The secondary phases in crystal sections or metasomatic replacement with decrease in Fe^{3+} and Mg^{2+}, yet increase in Na^+, indicate a further evolution and fractionation of the fluid in its late stage. This would support the hypothesis of early crystallisation of aquamarine with goshenite being late. These observations relate to the suggestion that goshenite is associated with highly evolved fluids, e.g. in pegmatites (Černý *et al.*, 2003; Neiva and Neiva, 2005; Wang *et al.*, 2009) and with the limited Fe^{3+} and A-site substitution not being of magmatic origin. These results are further consistent with the understanding that the Xuebaoding W–Sn–Be–F–P mineralisation is primarily hydrothermal in origin and derived from a highly evolved fluid emerging from the Pankou and Pukouling albite leucogranites that are highly fractionated, alkali, peraluminous, Li–F-enriched (Zhu *et al.*, 2020) giving rise to the beryl, cassiterite, scheelite, fluorite and apatite mineral assemblage.

The tabular habit is therefore unlikely to be related to chemical composition and alkali content. However, the factors that control crystal habit in this and other localities remain unknown. More plausible than a chemical effect is the role of pressure and temperature, giving rise to anisotropy in lattice compressibility and thermal expansion. That may control, not only the size of lattice sites affecting substitution, but also the free energy of and preferential growth along particular crystallographic directions. Understanding the relationship of crystal habit to chemical, pressure and temperature conditions of the source fluid would be a subject of considerable general importance.

References

Adamo I., Pavese A., Prosperi L., Diella V., Ajò D., Gatta G.D. and Smith C.P. (2008) Aquamarine, maxixe-type beryl, and hydrothermal synthetic blue beryl: analysis and identification. *Gems & Gemology*, **44**, 214–226.

Aines R.D. and Rossman G.R. (1984) Water in minerals? A peak in the infrared. *Journal of Geophysical Research: Solid Earth*, **89**, 4059–4071.

Armstrong J.T. (1988) Quantitative analysis of silicates and oxide minerals: comparison of Monte-Carlo, ZAF and Phi-Rho-Z procedures. Pp. 239–246 in: *Proceedings of Microbeam Analysis Society* (D.E. Newbury, editor). San Francisco Press, San Francisco.

Artioli G., Rinaldi R., Stahl K. and Zanazzi P.F. (1993) Structure refinements of beryl by single-crystal neutron and X-ray diffraction. *American Mineralogist*, **78**, 762–768.

Aurisicchio C., Fioravanti G., Grubessi O. and Zanazzi P. (1988) Reappraisal of the crystal chemistry of beryl. *American Mineralogist*, **73**, 826–837.

Aurisicchio C., Grubessi O. and Zecchini P. (1994) Infrared spectroscopy and crystal chemistry of the beryl group. *The Canadian Mineralogist*, **32**, 55–68.

Azavant P. and Lichanot A. (1993) X-ray scattering factors of oxygen and sulfur ions: an ab initio Hartree–Fock calculation. *Acta Crystallographica*, **A49**, 91–97.

Bakakin V.V., Rylov G.M. and Belov N.V. (1969) Crystal structure of a lithium-bearing beryl. *Doklady Akademii Nauk SSSR*, **188**, 659–662.

Belov N.V. (1958) Essays on structural mineralogy IX. *Mineralogicheskiy Sbornik L'vovskogo Obshchestva*, **12**, 15–42 [in Russian].

Bosi F., Hatert F., Hålenius U., Pasero M., Miyawaki R. and Mills S.J. (2019) On the application of the IMA-CNMNC dominant-valency rule to complex mineral compositions. *Mineralogical Magazine*, **83**, 627–632.

Cao Z., Zheng J., Li Y., Ren J., Xu S., Wang R., Shoji T., Kaneda H. and Kabayashi S. (2002) Geologic and geochemical features of the volatile-rich ore fluid and its tracing and dating in the Xuebaoding Beryl-Scheelite Vein Deposit, China. *Science in China, Series D: Earth Sciences*, **45**, 719–729.

Cao Z., Jianbin Z., An W. and Youguo L. (2004) Geochemistry of Xuebaoding alkali granite and its ore-controlling effect. *Journal of Ocean University of Qingdao*, **34**, 874–880.

Černý P. (1975) Alkali variations in pegmatitic beryls and their petrogenetic implications. *Neues Jahrbuch für Mineralogie – Abhandlungen*, **123**, 198–212.

Černý P. (2002) Mineralogy of beryllium in granitic pegmatites. Pp. 405–444 in: *Beryllium: Mineralogy, Petrology, and Geochemistry* (E.S. Grew, editor). Reviews in Mineralogy and Geochemistry, **50**. Mineralogical Society of America and the Geochemical Society, Chantilly, Virginia, USA.

Černý P., Anderson A.J., Tomascak P.B. and Chapman R. (2003) Geochemical and morphological features of beryl from the Bikita granitic pegmatite, Zimbabwe. *The Canadian Mineralogist*, **41**, 1003–1011.

Chantler C.T., Olsen K., Dragoset R.A., Chang J., Kishore A.R., Kotochigova S.A. and Zucker D.S. (2005) *X-Ray Form Factor, Attenuation, and Scattering Tables (Version 2.1)*. National Institute of Standards and Technology, Gaithersburg, MD, USA. [Online at http://physics.nist.gov/ffast, retrieved 2 August 2020].

Charoy B., De Donato P., Barres O. and Pinto-Coelho C. (1996) Channel occupancy in an alkali-poor beryl from Serra Branca (Goias, Brazil): Spectroscopic characterization. *American Mineralogist*, **81**, 395–403.

Chen Z., Wan S., Lu X. and Wang W. (2002) Study on fluid inclusions in beryl from Pingwu, Sichuan province. *Geological Science and Technology Information*, **21**, 65–73.

Cook R.B. (2011) Connoisseur's choice: Beryl, variety morganite San Diego County, California. *Rocks and Minerals*, **86**, 50–57.

Cromer D.T. and Mann J.B. (1968) X-ray scattering factors computed from numerical Hartree–Fock wave functions. *Acta Crystallographica*, **A24**, 321–324.

Della Ventura G., Radica F., Bellatreccia F., Freda C. and Cestelli Guidi M. (2015) Speciation and diffusion profiles of H_2O in water-poor beryl: comparison with cordierite. *Physics and Chemistry of Minerals*, **42**, 735–745.

Donovan J.J., Singer J.W. and Armstrong J.T. (2016) A new EPMA method for fast trace element analysis in simple matrices. *American Mineralogist*, **101**, 1839–1853.

Folinsbee R.E. (1941) Optic properties of cordierite in relation to alkalies in the cordierite-beryl structure. *American Mineralogist*, **26**, 485–500.

Fridrichová J., Bačík P., Rusinová P., Antal P., Škoda R., Bizovská V. and Miglierini M. (2015) Optical and crystal-chemical changes in aquamarines and yellow beryls from Thanh Hoa province, Vietnam induced by heat treatment. *Physics and Chemistry of Minerals*, **42**, 287–302.

Fridrichová J., Bačík P., Bizovská V., Libowitzky E., Škoda R., Uher P., Ozdín D. and Števko M. (2016) Spectroscopic and bond-topological investigation of interstitial volatiles in beryl from Slovakia. *Physics and Chemistry of Minerals*, **43**, 419–437.

Fukuda J. and Shinoda K. (2008) Coordination of water molecules with Na^+ cations in a beryl channel as determined by polarized IR spectroscopy. *Physics and Chemistry of Minerals*, **35**, 347–357.

Fukuda J. and Shinoda K. (2011) Water molecules in beryl and cordierite: High-temperature vibrational behavior, dehydration, and coordination to cations. *Physics and Chemistry of Minerals*, **38**, 469–481.

Fukuda J., Shinoda K., Nakashima S., Miyoshi N. and Aikawa N. (2009) Polarized infrared spectroscopic study of diffusion of water molecules along structure channels in beryl. *American Mineralogist*, **94**, 981–985.

Gatta G.D., Nestola F., Bromiley G.D. and Mattauch S. (2006) The real topological configuration of the extra-framework content in alkali-poor beryl: A multi-methodological study. *American Mineralogist*, **91**, 29–34.

Ginzburg A.I. (1955) On the question of the composition of beryl. *Trudy Mineralogicheskogo Muzeya, Akademiya Nauk*, **7**, 56.

Giuliani G., France-Lanord C., Zimmermann J.L., Cheilletz A., Arboleda C., Charoy B., Coget P., Fontan F. and Giard D. (1997) Fluid composition, δD of channel H_2O, and $\delta^{18}O$ of lattice oxygen in beryls: Genetic implications for brazilian, colombian, and afghanistani emerald deposits. *International Geology Review*, **39**, 400–424.

Goldman D.S., Rossman G.R. and Dollase W.A. (1977) Channel constituents in cordierite. *American Mineralogist*, **62**, 1144–1157.

Groat L.A., Giuliani G., Marshall D.D. and Turner D. (2008) Emerald deposits and occurrences: A review. *Ore Geology Reviews*, **34**, 87–112.

Groat L.A., Rossman G.R., Dyar M.D., Turner D., Piccoli P.M.B., Schultz A.J. and Ottolini L. (2010) Crystal chemistry of dark blue aquamarine from the true blue showing, Yukon territory, Canada. *The Canadian Mineralogist*, **48**, 597–613.

Guo Y., Wang R., Xu S., Fontan F., Luo Y. and Cao Z. (2000a) A study of the structure of a rare tabular crystal of beryl. *Geological Review*, **46**, 312–317.

Guo Y., Wang R. and Xu S. (2000b) Vibrational spectra of beryl from Xuebaoding, Pingwu County, Sichuan Province. *Geological Journal of China Universities*, **2**, 201–204.

Hagemann H., Lucken A., Bill H., Gysler-Sanz J. and Stalder H. (1990) Polarized Raman spectra of beryl and bazzite. *Physics and Chemistry of Minerals*, **17**, 395–401.

Hawthorne F.C. and Černý P. (1977) The alkali-metal positions in Cs-Li beryl. *The Canadian Mineralogist*, **15**, 414–421.

Jiang S., Zhou Y., Guo C., Cao Y. and Xu H. (2007) Fluid inclusions of the Pingwu W–Sn–Be deposit in Sichuan. *Geological Review*, **53**, 407–412.

Kim C.C., Bell M.I. and McKeown D.A. (1995) Vibrational analysis of beryl ($Be_3Al_2Si_6O_{18}$) and its constituent ring (Si_6O_{18}). *Physica B: Physics of Condensed Matter*, **205**, 193–208.

Kirby E. and Ouimet W. (2011) Tectonic geomorphology along the eastern margin of Tibet: insights into the pattern and processes of active deformation adjacent to the Sichuan Basin. Pp. 165–188 in: *Growth and Collapse of the Tibetan Plateau* (R. Gloaguen and L. Ratschbacher, editors). Geological Society, London, Special Publications, **353**.

Kolesov B.A. and Geiger C.A. (2000) The orientation and vibrational states of H₂O in synthetic alkali-free beryl. *Physics and Chemistry of Minerals*, **27**, 557–564.

Li J., Liu B., Wang D. and Fu X. (2007) Metallogenic epoch of Xubaoding W–Sn–Be deposit in northwest Sichuan and its tectonic tracing significance. *Mineral Deposits*, **26**, 557–562.

Lin J., Cao Z., Liu J., Li Y., Zhang Y. and Ying S. (2000) Mineral spectroscopic studies of beryls from Xuebaoding, Sichuan. *Acta Petrrologica et Mineralogica*, **19**, 369–375.

Liu Y., He M., Zhang D., Yu X. and Pan Z. (2001a) Gemmology of Beryl from Pingwu, Sichuan Province. *Journal of Gems & Gemmology*, **3**, 31–34.

Liu Y., Zhang B. and Yu X. (2001b) The mineralogical characteristics and its application prospect of beryl in Pingwu, Sichuan. *Geology and Prospecting*, **37**, 55–57.

Liu Y., Deng J., Cai K.Q., Zhou Y., Wang Q.F., Zhou Y.H., Gao B.F., De xiu L.I., Fu yu X.U. and Zhu Y.R. (2005) Mineralogical characteristics of beryl in Pingwu County, Sichuan Province, south-west China. *Earth Science Frontiers*, **12**, 324–331.

Liu Y., Deng J., Li G. and Shi G. (2007) Structure refinement of Cs-rich Na-Li beryl and analysis of its typomorphic characteristics of configurations. *Acta Geologica Sinica*, **81**, 61–67.

Liu Y., Deng J., Shi G. and Sun D. (2012) Geochemical and morphological characteristics of coarse-grained tabular beryl from the Xuebaoding W–Sn–Be deposit, Sichuan Province, western China. *International Geology Review*, **54**, 1673–1684.

Łodziński M., Sitarz M., Stec K., Kozanecki M., Fojud Z. and Jurga S. (2005) ICP, IR, Raman, NMR investigations of beryls from pegmatites of the Sudety Mts. *Journal of Molecular Structure*, **744–747**, 1005–1015.

Lum J.E., Viljoen F., Cairncross B. and Frei D. (2016) Mineralogical and geochemical characteristics of beryl (aquamarine) from the Erongo Volcanic Complex, Namibia. *Journal of African Earth Sciences*, **124**, 104–125.

Mashkovtsev R.I., Thomas V.G., Fursenko D.A., Zhukova E.S., Uskov V. V. and Gorshunov B.P. (2016) FTIR spectroscopy of D₂O and HDO molecules in the *c*-axis channels of synthetic beryl. *American Mineralogist*, **101**, 175–180.

Mihalynuk M.G. and Lett R. (2003) Composition of Logtung beryl (aquamarine) by ICPES/MS: a comparison of beryl worldwide. Pp. 141–146 in: *Geological Fieldwork*. Crown Publications Inc., British Columbia, Canada.

Neiva A.M.R. and Neiva J.M.C. (2005) Beryl from the granitic pegmatite at Namivo, Alto Ligonha, Mozambique. *Neues Jahrbuch für Mineralogie – Abhandlungen*, **181**, 173–182.

Ottens B. (2005) Xuebaoding: Pingwu County, Sichuan Province, China. *Mineralogical Record*, **36**, 45–57.

Pankrath R. and Langer K. (2002) Molecular water in beryl, $^{VI}Al_2$ $[Be_3Si_6O_{18}]$ ·nH₂O, as a function of pressure and temperature: An experimental study. *American Mineralogist*, **87**, 238–244.

Pauly C. (2019) *Mineralogy and Petrogenesis of the California Blue Mine Aquamarine- and Topaz-Bearing Pegmatite Deposit, San Bernardino County, California*. Colorado School of Mines, USA.

Qi L., Ye S., Xiang C., Pei J. and Luo Y. (2001a) Color center and coloring mechanism of irradiated beryl. *Geological Science and Technology Information*, **20**, 68–72.

Qi L., Pei J., Zhou K., Shi G. and Luo Y. (2001b) Crystal defect and growth mechanism of alkali-rich beryl crystal from Pingwu, Sichuan, China. *Geological Science and Technology Information*, **20**, 64–70.

Qi L., Xiang C., Liu G., Pei J. and Luo Y. (2001c) ESR behaviour of paramagnetic mixture in irradiated beryl. *Geological Science and Technology Information*, **20**, 59–64.

Qi L., Ye S., Xiang C., Pei J. and Shi G. (2001d) Vibration spectrum and irradiation splitting of mixture in beryl channels. *Geological Science and Technology Information*, **20**, 59–64.

Robinson K., Gibbs G.V. and Ribbe P.H. (1971) Quadratic elongation: a quantitative measure of distortion in coordination polyhedra. *Science*, **172**, 567–570.

Roger F., Malavieille J., Leloup P.H., Calassou S. and Xu Z. (2004) Timing of granite emplacement and cooling in the Songpan–Garzê fold belt (eastern Tibetan Plateau) with tectonic implications. *Journal of Asian Earth Sciences*, **22**, 465–481.

Roger F., Jolivet M. and Malavieille J. (2010) The tectonic evolution of the Songpan-Garzê (North Tibet) and adjacent areas from Proterozoic to Present: A synthesis. *Journal of Asian Earth Sciences*, **39**, 254–269.

Sardi F.G. and Heimann A. (2014) Pegmatitic beryl as indicator of melt evolution: example from the Belasco district, Pampeana pegmatite province, Argentina, and review of worldwide occurrences. *The Canadian Mineralogist*, **52**, 809–836.

Scandale E. and Lucchesi S. (2000) Growth and sector zoning in a beryl crystal. *European Journal of Mineralogy*, **12**, 357–366.

Scandale E., Lucchesi S. and Graziani G. (1990) Growth defects and growth marks in pegmatite beryls. *European Journal of Mineralogy*, **2**, 305–312.

Sheldrick G.M. (2008) A short history of SHELX. *Acta Crystallographica*, **A64**, 112–122.

Sherriff B.L., Grundy H.D., Hartman J.S., Hawthorne F.C. and Černý P. (1991) The incorporation of alkalis in beryl; a multinuclear MAS NMR and crystal-structure study. *The Canadian Mineralogist*, **29**, 271–285.

Sunagawa I. (1984) *Growth of crystals in nature*. Pp. 61–103 in: *Materials Science of the Earth's Interior*. Terra Scientific Publishing, Tokyo.

Tempesta G., Scandale E. and Agrosì G. (2011) Striations and hollow channels in rounded beryl crystals. *Periodico di Mineralogia*, **79**, 75–87.

Tempesta G., Bosi F. and Agrosì G. (2020) Crystal chemical characterisation of red beryl by 'Standardless' laser-induced breakdown spectroscopy and single-crystal refinement by X-Ray diffraction: An example of validation of an innovative method for the chemical analysis of minerals. *Geostandards and Geoanalytical Research*, **44**, 685–693.

Uher P., Chudík P., Bačík P., Vaculovič T. and Galliová M. (2010) Beryl composition and evolution trends: an example from granitic pegmatites of the beryl-columbite subtype, Western Carpathians, Slovakia. *Journal of Geosciences*, **55**, 69–80.

Wang R., Cheng Che X., Dong Zhang W., Lan Zhang A. and Cheng Zhang H. (2009) Geochemical evolution and late re-equilibration of NaCs-rich beryl from the Koktokay #3 pegmatite (Altai, NW China). *European Journal of Mineralogy*, **21**, 795–809.

Wood D.L. and Nassau K. (1967) Infrared spectra of foreign molecules in beryl. *The Journal of Chemical Physics*, **47**, 2220–2228.

Wood D.L. and Nassau K. (1968) The characterization of beryl and emerald by visible and infrared absorption spectroscopy. *American Mineralogist*, **53**, 777–800.

Xiao L., Zhang H.F., Clemens J.D., Wang Q.W., Kan Z.Z., Wang K.M., Ni P.Z. and Liu X.M. (2007) Late Triassic granitoids of the eastern margin of the Tibetan Plateau: Geochronology, petrogenesis and implications for tectonic evolution. *Lithos*, **96**, 436–452.

Xu Z., Hou L., Wang Z., Fu X. and Huang M. (1992) *Orogenic Processes of the Songpan Ganze Orogenic Belt of China*. Geological Publishing House, Beijing.

Yakubovich O.V., Pekov I.V., Steele I.M., Massa W. and Chukanov N.V. (2009) Alkali metals in beryl and their role in the formation of derivative structural motifs: Comparative crystal chemistry of vorobyevite and pezzottaite. *Crystallography Reports*, **54**, 399–412.

Ye S., Qi L., Luo Y., Zhou K. and Pei J. (2001) Relationship between the rare-metal contained granitic intrusions and beryl mineralization in Pingwu, Sichuan, China. *Geological Science and Technology Information*, **20**, 65–70.

Zhang D., Peng J., Coulson I.M., Hou L. and Li S. (2014) Cassiterite U-Pb and muscovite ^{40}Ar–^{39}Ar age constraints on the timing of mineralization in the Xuebaoding Sn-W-Be deposit, western China. *Ore Geology Reviews*, **62**, 315–322.

Zhang L., Ruan Q. and Rao C. (2012) The crystal growth and characteristics of etched figures on c{0001} face of tabular beryl crystal from Pingwu, China. *Acta Mineralogica Sinica*, **32**, 1–8.

Zhou K., Qi L., Xiang C., Feng Q., Wu J. and Hao Q. (2002) Geologic characteristic of forming beryl gem from Pingwu Sichuan. *Journal of Mineralogy and Petrology*, **22**, 1–7.

Zhu X., Raschke M.B. and Liu Y. (2020) Tourmaline as a recorder of ore-forming processes in the Xuebaoding W–Sn–Be deposit, Sichuan province, China: Evidence from the chemical composition of tourmaline. *Minerals*, **10**, 438.